Cretaceous Research 110 (2020) 104384

Contents lists available at ScienceDirect

Cretaceous Research

journal homepage: www.elsevier.com/locate/CretRes

A refined temporal framework for newly discovered fossil assemblages of the upper Cedar Mountain Formation (Mussentuchit Member), Mussentuchit Wash, Central Utah

Ryan T. Tucker [a,*], Lindsay E. Zanno [b,c], Hui-Qing Huang [d], Peter J. Makovicky [e]

[a] *Department of Earth Sciences, Stellenbosch University, Private Bag X1 Matieland, Stellenbosch, 7602, South Africa*
[b] *Paleontology, North Carolina Museum of Natural Sciences, 11 W. Jones St., Raleigh, NC, 27601, USA*
[c] *Department of Biological Sciences, Campus Box 7617, North Carolina State University, Raleigh, NC, 27695, USA*
[d] *Economic Geology Research Center, College of Science and Engineering, Division of Tropical Environments and Societies, James Cook University, Townsville, QLD, 4811, Australia*
[e] *Department of Earth and Environmental Sciences, University of Minnesota, Minneapolis, MN, 55455, USA*

A R T I C L E I N F O

Article history:
Received 18 September 2019
Received in revised form
10 January 2020
Accepted in revised form 14 January 2020
Available online 23 January 2020

Keywords:
Cedar Mountain Formation
Mussentuchit Wash
Mussentuchit Member
U–Pb geochronology
Chronostratigraphy

A B S T R A C T

Detangling the pace and structure of biotic turnover between the late Early and early Late Cretaceous within the Western Interior of North America requires refined stratigraphic controls of fossiliferous sediments; however, to date, many key mid-Cretaceous strata remain understudied and only tenuously or coarsely correlated. Intensified data collection in the uppermost Cedar Mountain Formation (Mussentuchit Member) suggests preservation of an understudied volcanilithic archive that can provide key insight into this enigmatic period in North America's geological history. Here we utilize detrital zircon geochronology (coupling LA-ICP-MS and CA-TIMS) to contextualize the sedimentary history of the Mussentuchit Member within the region of Mussentuchit Wash, Central Utah and compare these data with previous approaches. This study finds that emplacement of contemporaneous volcanilithics occurred in two distinct phases. The first phase occurred no older than 96 Ma, and a subsequent younger phase occurred no older than 94 Ma. Secondly, this study finds preliminary evidence that both eruptions occurred within a westerly lying arc; however, it is evident that these represent different volcanic inliers and terranes. Finally, this study also finds that the Mussentuchit Member can be reliably subdivided into two informal lower and upper sub-members, with the potential to preserve two distinct, previously unified fossil assemblages. Our data provides both a refined localized framework for newly uncovered fossil assemblages within this particular Mussentuchit Wash depo-centre and serves to strengthen correlations between mid-Cretaceous strata across the Western Interior.

1. Introduction

The Cretaceous Western Interior Basin (WIB, the sedimentary basin eastward of the Sevier Mountain Range) preserves one of the most continuous records of terrestrial life during the Early to Late Cretaceous transition. The “mid-Cretaceous” (125–90 Myr) a period of global environmental change known for atmospheric temperature increases, rising seas, shrinking continental habitats, diversification of flowering plants, and dramatic turnover in vertebrate life (Hedges et al., 1996; Dilcher, 2000; Skelton et al., 2003; Fastovsky et al., 2004; Weishampel et al., 2004; Lloyd et al., 2008; Slattery et al., 2015; Scott et al., 2018). Several decades of research on the WIB have established a general chronostratigraphic framework for fossil assemblages in the mid-Cretaceous (Kauffman and Caldwell, 1993; Sames et al., 2010; Eldrett et al., 2015; Morath et al., 2015; D'Emic et al., 2019; Miall and Catuneanu, 2019) and revealed that periodic connections between the continents of North America and Asia had a profound impact on the establishment of a distinctly different terrestrial ecosystem on the continent (e.g., Cifelli et al., 1997; Kirkland et al., 1997, 1999; Zanno and Makovicky, 2011, 2013; Makovicky et al., 2014; Nesbitt et al., 2019; Zanno and Makovicky, 2019). Originally represented as a faunal turnover with endemic lineages replaced by clades immigrating from Asia (Cifelli et al., 1997; Kirkland and Farlow, 2012),

* Corresponding author.
E-mail address: tucker@sun.ac.za (R.T. Tucker).

https://doi.org/10.1016/j.cretres.2020.104384
0195-6671/

recent data suggests that this event occurred over a prolonged period (Zanno and Makovicky, 2011; Makovicky et al., 2015) and that chronostratigraphic resolution within and between many mid-Cretaceous formations is insufficient to tease apart complexities in paleobiogeographic trends as well as the pace and structure of floral and faunal replacement patterns. Stratigraphic comparisons in the WIB are currently hindered by inconsistencies within terrestrial biostratigraphic frameworks, the Cretaceous Long Normal Superchron (±121–83 Myr), dating by different radiometric techniques (e.g., U–Pb versus Ar–Ar), and stratigraphic inconsistencies due to the wide array of depo-centres preserved within sub-basins of the Western Interior (Jinnah et al., 2009; Dickinson and Gehrels, 2008; Laskowski et al., 2013; D'Emic et al., 2019; Miall and Catuneanu, 2019).

Among mid-Cretaceous formations of the WIB, the Cedar Mountain Formation of Utah stands out as an exemplary model for investigating the pace and timing of these floral and fauna changes because it is highly fossiliferous and known to span approximately 30 million years or more, bracketing this interval and capturing all but the latest stages (Turonian) of this complex event (Arens and Harris, 2015; Kirkland et al., 2016; and references therein). Strata of the Cedar Mountain Formation are preserved within the San Rafael Swell, located along the distal backbulge to eventual forebulge of the Sevier fold-thrust belt, and lying east of the Cordilleran Arc (Yingling and Heller, 1992; DeCelles et al., 1995; DeCelles and Currie, 1996; Suarez et al., 2017) (Fig. 1). These localized depo-centres provide an archive for post- and near-to syndepositional volcaniclastics along with asynchronous epiclastic detritus from Cordilleran volcanic Phases; A (160–140 Myr), B (140–105 Myr), and even Phase C (105–80 Myr) (DeCelles and Graham, 2015). The ubiquity and longevity of detrital zircon within sedimentary systems of the WIB provide a rare opportunity to constrain depositional events within the Cedar Mountain Formation, along with the fossil assemblages therein (Fedo et al., 2003; Roberts, 2007; Dickinson and Gehrels, 2009a,b; Lawton et al., 2010; Gehrels, 2011).

Current lithostratigraphic subdivision of the Cedar Mountain Formation was described by Kirkland et al. (2016), and includes six regionally variable members from oldest to youngest: 1) Buckhorn Conglomerate; 2) Yellow Cat; 3) Poison Strip Sandstone 4) Ruby Ranch; 5) Short Canyon Conglomerate; and lastly 6) Mussentuchit Member (Hunt et al., 2011) (Fig. 2). Early studies indicated a Barremian-Albian age for the formation (Katich, 1951; Stokes, 1952; Simmons, 1957; DeCelles and Burden, 1992; Kirkland, 1992; DeCelles and Coogan, 2006) (Figs. 2 and 3). This included early work by Tschudy et al. (1984) within the area of Mussentuchit Wash which was constrained by key palynological assemblages of the youngest member of the Cedar Mountain Formation (the Mussentuchit Member) to the late Albian. Subsequent age dating of its individual members, and the overlying Naturita Sandstone (Dakota Sandstone of older literature), extended the depositional interval into the Cenomanian and identified numerous disconformities and unconformities within the Cedar Mountain Formation (Lawton et al., 2010; Hunt et al., 2011; Kirkland et al., 2016; and references therein). This age placement was biostratigraphically supported by Nichols and Sweet (1993) and Arens and Harris (2015), who considered the paleobotanical record of the Mussentuchit Member to be of late Albian to early Cenomanian (100–96 Myr) with the presence of pteridophytes (ferns) including *Gleicheniidites senonicus* and *Pityosprites*, along with gymnosperm pollen *Corollina torosa* and *Pilosisporites trichopapillosus*.

The last decade and a half have seen several attempts to assess the depositional age of the Cedar Mountain Formation as a whole with age dates ranging from Cenomanian to Berrisian. They include, but are not limited to studies to Britt et al. (2007, 2009), Burton et al. (2006), Chure et al. (2010), Garrison et al. (2007), Greenhalgh and Britt (2007), Hendrix et al. (2015), Ludvigson et al. (2010), Sprinkel et al. (2012). Some of the earliest radiometric dates from the Mussentuchit Member of the Cedar Mountain Formation were published by Cifelli et al. (1997) and Cifelli et al. (1999). Based on recovered sanidine phenocrysts from smectitic ash horizons, the upper portions of the Cedar Mountain Formation were emplaced around 98.39 ± 0.07 Ma ($^{40}Ar/^{39}Ar$), which was in close agreement with prior studies by Obradovich (1993; 98.5 Ma) and Gradstein et al. (1995; 98.9 ± 0.6 Ma) (Cifelli et al., 1999). In a later study by Garrison et al. (2007, pg 475), ash horizons near the Cifelli #2 fossil site were noted to have been recalculated via MMhb (age of 513.9Ma) to be slightly younger, at 97.0 ± 0.1 Ma. Further work by Garrison et al. (2007) at Cifelli #2, sampled and age dated plagioclase ($^{40}Ar/^{39}Ar$; via MMhb-1) from three separate ash horizons. The lowermost unit was reported to be at

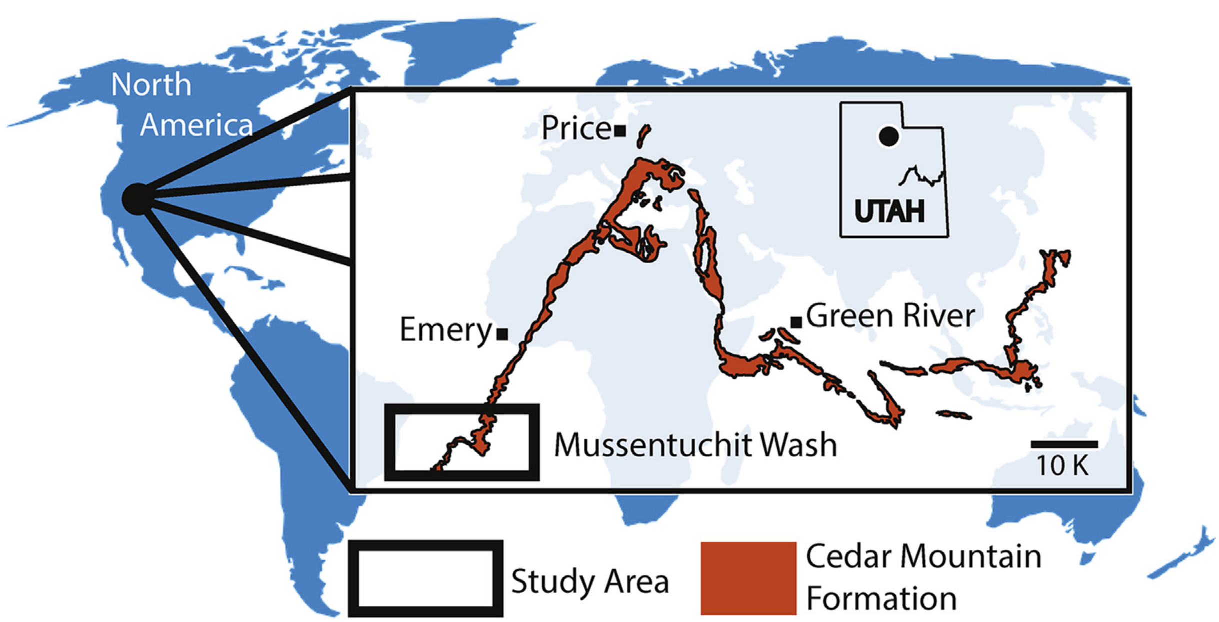

Fig. 1. Location of the exposed Cedar Mountain Formation across Central to East-central Utah, with study area (Mussentuchit Wash) indicated by the bold square.

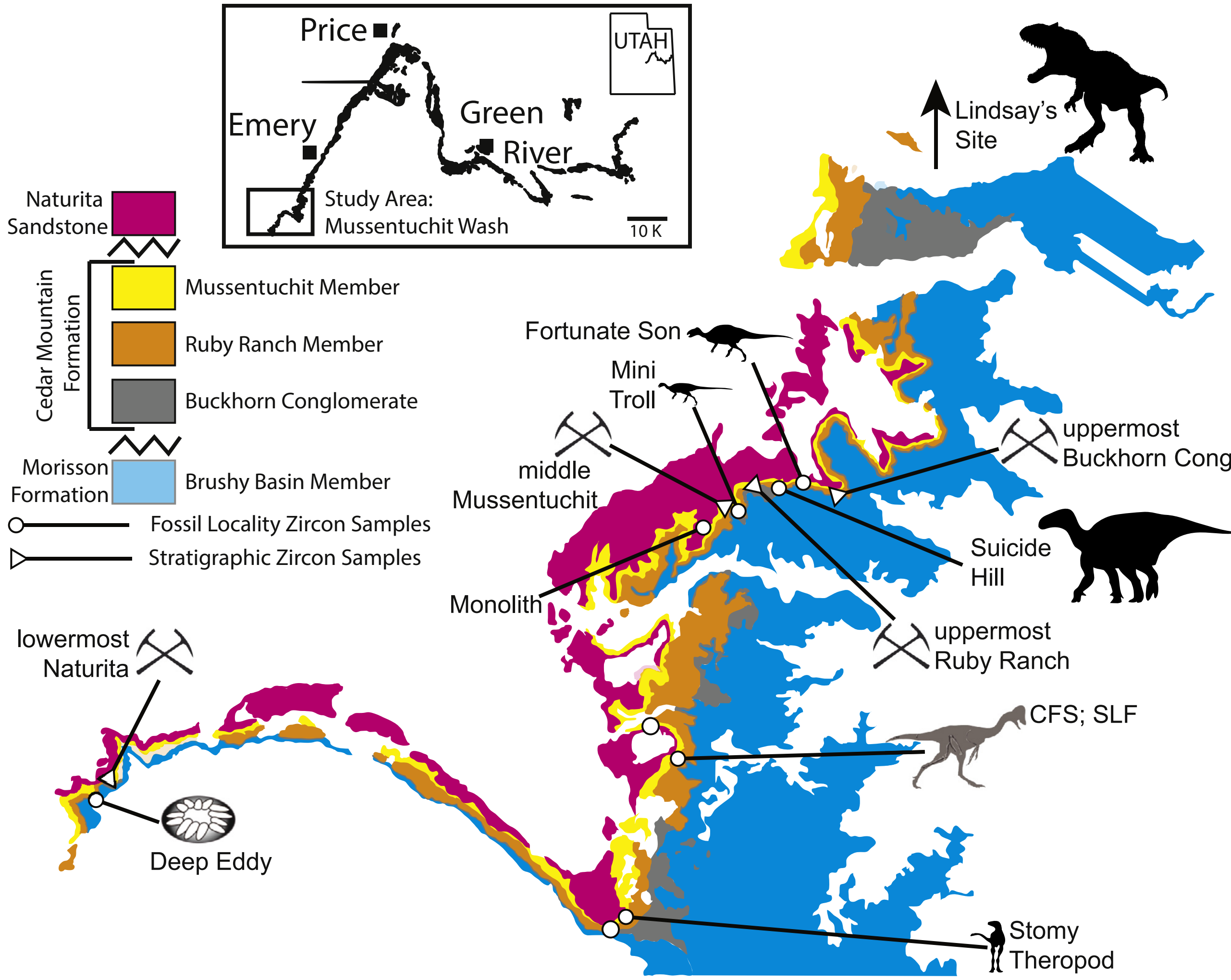

Fig. 2. Exposed members of the Cedar Mountain Formation in the Mussentuchit Wash, along with the underlying uppermost Brushy Basin Member (Morrison Formation) and the overlying Naturita Sandstone. Also indicated is the locations where zircon samples were collected.

98.5 ± 0.6 Ma, the medial unit at 96.7 ± 0.5 Ma, and the uppermost at 97.2 Ma. The three ash layers reported by Garrison et al. (2007) are out of temporal order (noted to be "discordant" (Garrison et al., 2007; pg 476)) possibly indicating reworking of the units rather than displaying contemporaneity between sedimentation and volcanic activity (May et al., 2013; Rossignol et al., 2019).

Between 2008 and the present, extensive surveys of the dinosaurian fauna of the Mussentuchit Member have been undertaken in the region of Mussentuchit Wash (here defined as the region of Mussentuchit outcrop spanning from the cliffs flanking the western margin of Last Chance Desert north to Mesa Butte) (Figs. 1 and 2). This decade of work has resulted in the discovery of several new vertebrate species and specimens (Zanno and Makovicky, 2013; Makovicky et al., 2014, 2015; Herzog et al., 2015; Zanno and Makovicky, 2016; Driebergen et al., 2017; Johnson-Ransom et al., 2017; Zanno et al., 2019; Avrahami et al., 2019) and a dramatic increase in the number of localities preserving taxonomically identifiable remains. Here we establish a temporal framework via radiometric age dating (LA-ICP-MS and CA-TIMS) of volcanilithic-rich detrital zircon and place newly discovered taxa into a refined temporal context (including several holotype localities). These new data are a first step in refining first and last appearance dates for vertebrate taxa of the Mussentuchit Member during the mid-Cretaceous turnover.

2. Regional background & lithology

Initially formed as an expansive foreland basin, the Western Interior Basin (WIB) is currently dissected into a mosaic of subbasins as a consequence of orogenic events (155–35 Myr) (Greenhalgh & Britt, 2007; Roca and Nadon, 2007). Later phases of this deformation included the thin-skinned Sevier fold-thrust belt and the younger basement-core uplifts of the Laramide Orogeny (Willis, 1999). Of particular relevance to this study is the coeval thrust-load (Pavant Thrust) generated flexural subsidence associated with deformation in the Sevier Thrust Belt (Currie, 2002). Eastward migration of the forebulge and the foredeep resulted in the uppermost Jurassic Morrison Formation and lowermost units of the Cedar Mountain Formation to be emplaced within the backbulge; whereas, units of the uppermost Cedar Mountain Formation were emplaced within the foredeep (Currie, 1997).

The lower contact of the Mussentuchit Member is regionally variable; either overlying the Short Canyon Member (chert-pebble lag) to the north or the Ruby Ranch Member (muddy, carbonate nodule-rich) to the south. Regionally, the Mussentuchit Member underlies and is likely down-cut or even interfingers with the Naturita Sandstone (Dakota Sandstone), or if the latter is eroded The Mussentuchit Member is overlain by the lowermost Tununk Member of the Mancos Shale (Leckie et al., 1997; Eberth et al., 2006;

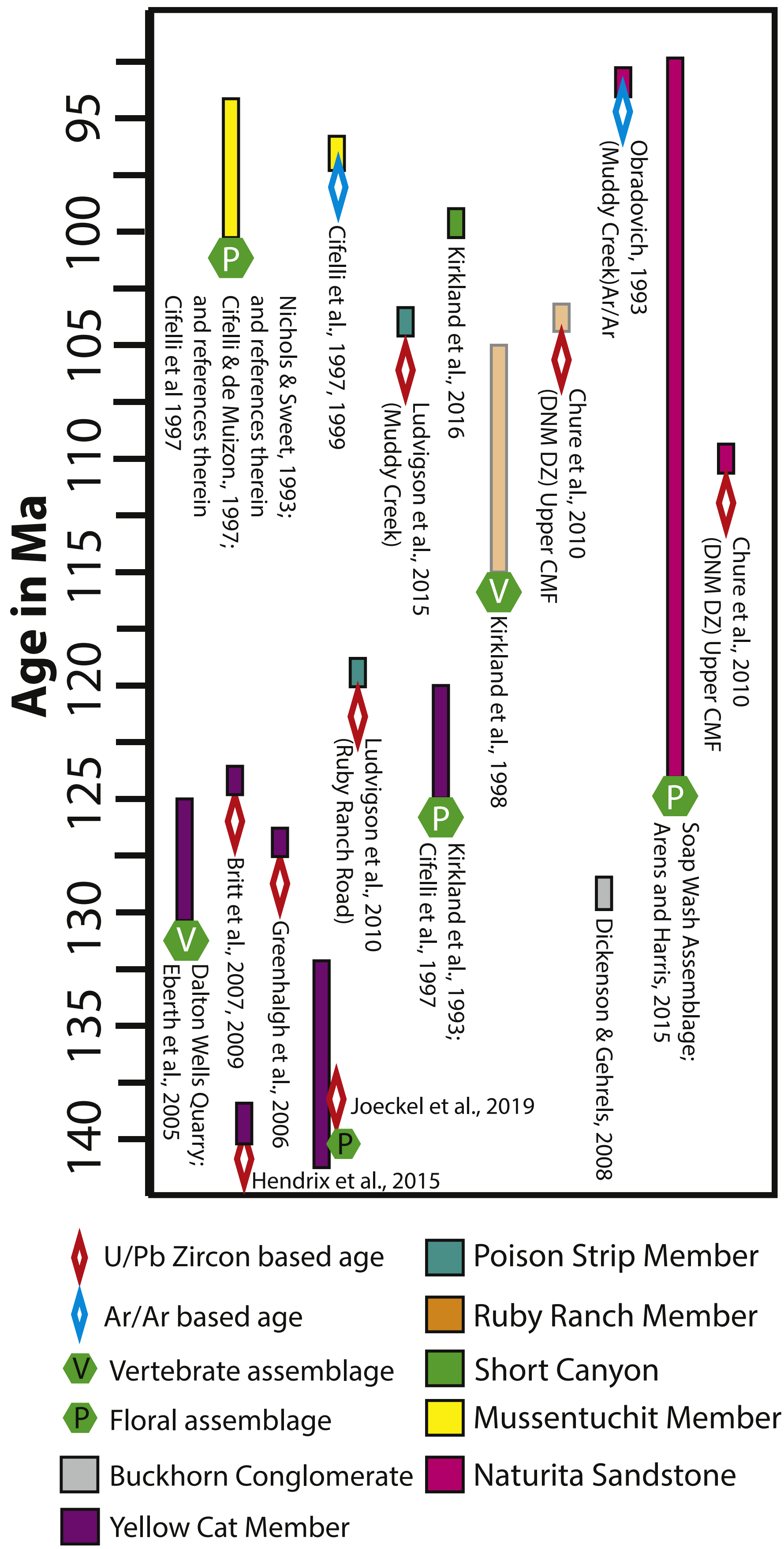

Fig. 3. Previous published temporal placement of stratigraphic units within the Cedar Mountain Formation, including but not limited to: The Buckhorn Conglomerate, Upper and Lower Yellow Cat Member, Poison Strip Member, Ruby Ranch Member, Short Canyon informal member, Mussentuchit Member, along with the overlying Naturita. (For interpretation of the references to colour in this figure legend, the reader is referred to the Web version of this article). (Bhattacharya and MacEachern, 2009; Blakey, 2014; Dickinson and Gehrels, 2010; Elderbak et al., 2014; Joeckel et al., 2019; Lockshin et al., 2017; Ludvigson et al., 2015; Shang et al., 2018; Suarez et al., 2014).

Kirkland and Madsen, 2007; Kirkland et al., 2016; Zanno et al., 2019). Locally, in the Mussentuchit Wash, the Mussentuchit is laterally continuous throughout the study area and averages ±25.0–40.0 m in total thickness (Fig. 4). Exposed sections of the Mussentuchit Member are composed of alternating drab grey to light grey silty-mudstones and muddy-siltstones. Predominantly, thin-to thick-bedded volcanilithic-rich (smectitic clays) clay-rich mudstones occur in the lower Mussentuchit, and volcanilithic-rich (smectitic clays) silt-rich mudstones dominate the upper Mussentuchit, coarsening upwards. Channelized lenticular fine to medium-grained sandstones are identified and occur more commonly in the middle and upper Mussentuchit. Other structures include abandoned channels, channel splays, and both ephemeral channels and saline ponds. Commonly associated with these sediments are coalified plant hash, variably preserved shell hash, and both syngenetic and diagenetic gypsum and anhydride.

3. Methods

3.1. Stratigraphy and sedimentation

All samples were collected in the area surrounding Mussentuchit Wash, Central Utah, along the southwestern corridor of the exposed Cedar Mountain Formation. Seven fossil localities were investigated during this project, including 1) Fortunate Son; 2) Stormy Theropod (the holotype locality for *Moros intrepidus*); 3) Mini Troll; 4) Suicide Hill; 5) Deep Eddy; 6) Lindsay's Site (the holotype locality for *Siats meekerorum*) and 7) SLF (Fig. 4). A further four samples were collected from key stratigraphic positions including: 1) the uppermost Buckhorn Conglomerate; 2) the uppermost Ruby Ranch; 3) “middle” Mussentuchit; and 4) the lowermost Naturita (Fig. 4).

Sedimentologic analysis of the Cedar Mountain Formation and its members was conducted between 2014 and 2018, with work ongoing. Detailed facies and architectural element analysis was performed following the conceptual framework established by Miall (1977, 1985, 2014) and modified by Eberth and Miall (1991), Roberts (2007), Jinnah et al. (2009), Reading (2009) and Tucker et al. (2013, 2017). For consistency, a uniform set of facies codes was utilized to best describe the outcrop sections. Detailed measured sections were constructed at the decimetre scale in each of the study areas using a Jacob's Staff, Brunton Compass, and GPS. Particular emphasis was placed on understanding and correlating important vertebrate fossil localities in each study area. Many horizons were walked out in order to define the horizontal and lateral continuity of beds and facies.

3.2. Geochronology

3.2.1. LA-ICP-MS

Eleven samples for detrital zircon geochronology via LA-ICP-MS were collected at key fossil localities or specific stratigraphic levels within each member of the Cedar Mountain Formation in the Mussentuchit Wash (Fig. 4). The lowest samples were collected in the underlying uppermost Buckhorn Conglomerate and uppermost Ruby Ranch, with two further samples collected from the middle Mussentuchit and the overlying lowermost Naturita Sandstone. The remaining samples were collected from previously excavated fossil sites (<10 yrs).

All zircons were isolated from the samples by mineral separation techniques at the Central Analytical Facilities, Stellenbosch University, making use of standard methods for crushing, milling, panning, Frantz magnetic separation and dense liquid separation. All laser ablation U–Pb data was collected at the Central Analytical Facilities, Stellenbosch University, using a 193 nm wavelength ASI Resolution laser ablation system coupled to a Thermo Scientific Element 2 single collector magnetic sector field inductively coupled plasma mass spectrometer (SC-SF-ICP-MS).

At the start of each analytical session the mass spectrometer was tuned by ablating a line scan on the NIST620 glass. The torch position, lenses and gas flows were tuned while measuring ^{206}Pb, ^{238}U and ^{238}U^{16}O to get stable signals and high intensity on ^{206}Pb and ^{238}U, as well as low oxide rates (^{238}U^{16}O/^{238}U < 0.3%). The ablated zircon material was transported from the laser cell into the ICP-MS using a continuous flow of 0.35 l/min of He gas. Signals of m/z 202, 204, 206, 207, 208, 232, 235 and 238 were acquired in electrostatic scan mode. The ^{202}Hg signal was collected in order to correct the isobaric interference of ^{204}Hg on ^{204}Pb. The laser and ICP-MS software packages were synchronized in order to allow automated execution of the analysis. One analytical session can include up to 500 measurements.

Laser sampling protocol for samples Deep Eddy, Fortunate Son, lowermost Naturita and uppermost Ruby Ranch (in 2018) employed a 26 μm static spot and a fluence of 2.0 J/cm^2. Before the gas blank measurement, each spot was pre-ablated by firing two laser shots to remove common Pb from the surface that may have been introduced during the sample preparation.

During each analytical session, the zircon reference materials GJ-1 (Jackson et al., 2004) and Plešovice (Sláma et al., 2008) were measured between groups of unknowns. Zircon GJ-1 was used as a matrix-matched primary reference material to correct for mass discrimination on measured isotope ratios in unknown samples and simultaneous correction for instrumental drift. The values used for normalization are based on ratios determined by ID-TIMS reported in Horstwood et al. (2016). Plešovice zircon was used as secondary reference material to validate the results and assess the quality of the data for each analytical session. Data reduction was performed with the software package Iolite v.3.5 (Paton et al., 2011), combined with VizualAge (Petrus and Kamber, 2012). An exponential model of laser-induced elemental fractionation (LIEF) obtained by combining the isotopic ratios of the primary reference material from the entire session is used to correct for time-dependent, down-hole elemental fractionation in the unknowns, under the assumption of same fractionation behaviour in the reference material and the unknowns. After correction for LIEF and drift and normalization to the main reference material (performed in Iolite), uncertainty components for systematic errors are propagated by quadratic addition following the recommendations of Horstwood et al. (2016). Minor differences are noted for laser sampling protocol for all other samples (between 2016 and 2017), which employed a 25 or 30 μm static spot and a fluence of 1.4 J/cm^2. During each analytical session, the zircon reference materials GJ-1 (Jackson et al., 2004), Plešovice (Sláma et al., 2008), and M127 (Nasdala et al., 2016) were measured between groups of unknowns. Data reduction was performed with the software package Iolite v.3.5 (Paton et al., 2011), combined with VizualAge (Petrus and Kamber, 2012). For samples ablated in 2018, quality assurance was cross-checked by staff at the Central Analytical Facility at Stellenbosch University, whereas samples ablated in 2016–2017 were secondarily reduced by co-author at the Advanced Analytical Centre, James Cook University. Secondary analysis utilized Iolite v3.63 for data reduction using the U–Pb-Geochron4 data reduction scheme (similar to that described in Paton et al., 2011).

During ablation, for all samples, groups of 10–16 zircons were analyzed followed by at least two analyses of primary and secondary standards. If grains exhibited a greater discordance then 15%, those grains were omitted from the population as a whole (see Tucker et al., 2013, 2016; and references therein). All standard analyses were within 10% of the expected age, with most being within 5%. For samples Deep Eddy, Fortunate Son, lowermost Naturita, and

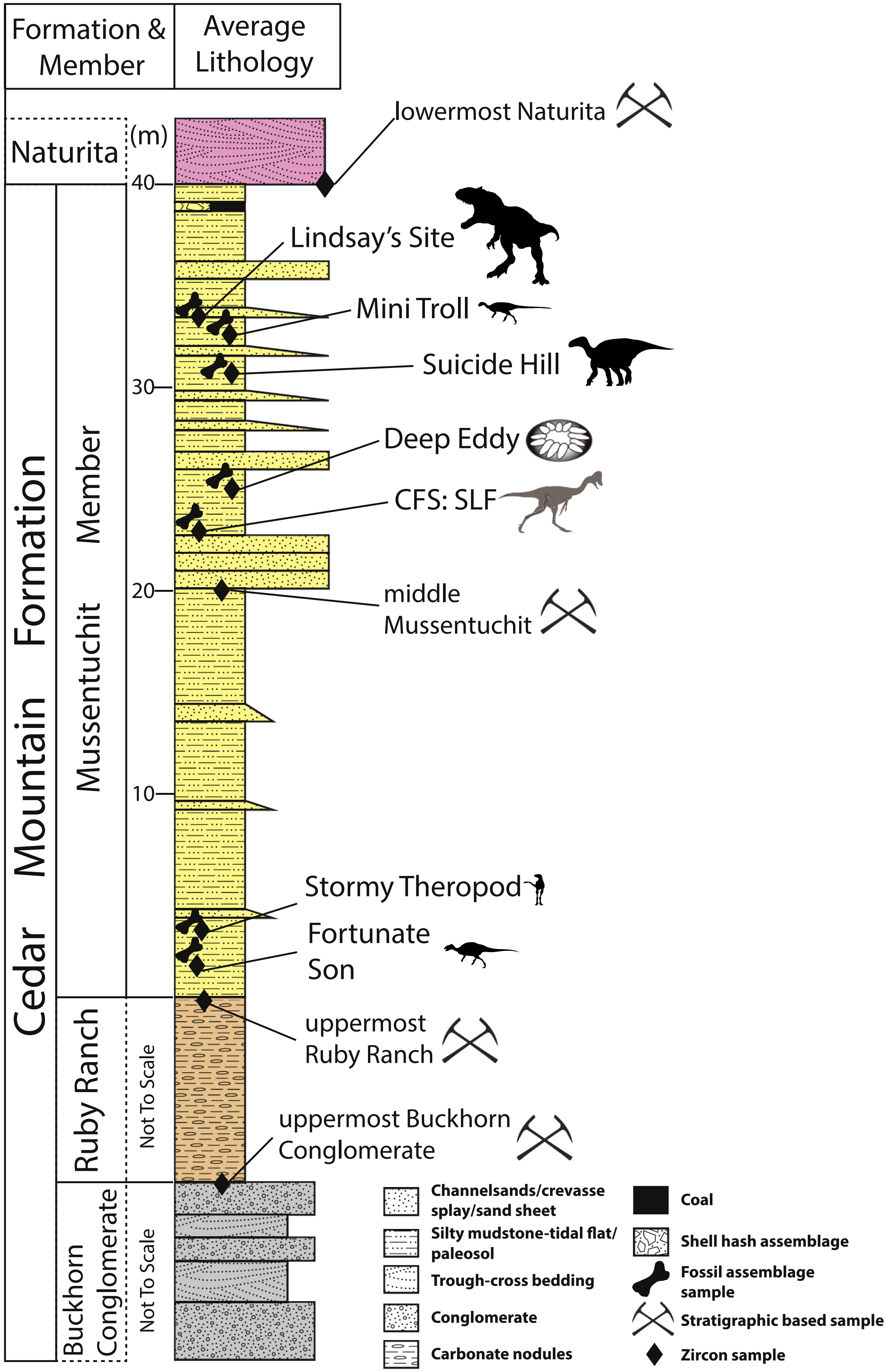

Fig. 4. Stratigraphic position of zircon samples collected from both active and historical localities along with stratigraphic position of zircon samples collected from key units in the Cedar Mountain Formation.

uppermost Ruby Ranch, instrument tuning is tabulated in Supplementary Table 1 and for all other samples, instrument tuning is tabulated in Supplementary Table 2.

The interpretation of the U–Pb data reported here were carried out solely by the authors of this paper.

3.2.2. CA-TIMS U–Pb

All zircons were secondarily processed at the Isotope Geology Laboratory (IGL), at Boise State University. U–Pb dates were obtained by the chemical abrasion isotope dilution thermal ionization mass spectrometry (CA-TIMS) method from analyses composed of single zircon grains (Table 1), modified after Mattinson (2005). Previously ablated zircon grains were plucked from the original grain mounts and placed in a muffle furnace at 900 °C for 60 h in quartz beakers. Zircon was put into 3 ml Teflon PFA beakers and loaded into 300 ml Teflon PFA microcapsules. Fifteen microcapsules were placed in a large-capacity Parr vessel and the zircon partially dissolved in 120 ml of 29 M HF for 12 h at 190 °C. Zircon was returned to 3 ml Teflon PFA beakers, HF was removed, and zircon was immersed in 3.5 M HNO_3, ultrasonically cleaned for an hour, and fluxed on a hotplate at 80 °C for an hour. The HNO_3 was removed and zircon was rinsed twice in ultrapure H_2O before being reloaded into the 300 ml Teflon PFA microcapsules (rinsed and fluxed in 6 M HCl during sonication and washing of the zircon) and spiked with the EARTHTIME mixed ^{233}U–^{235}U–^{205}Pb tracer solution. Zircon was dissolved in Parr vessels in 120 ml of 29 M HF with a trace of 3.5 M HNO_3 at 220 °C for 48 h, dried to fluorides, and re-dissolved in 6 M HCl at 180 °C overnight. U and Pb were separated from the zircon matrix using an HCl-based anion-exchange chromatographic procedure (Krogh, 1973), eluted together and dried with 2 μl of 0.05 N H_3PO_4.

Pb and U were loaded on a single outgassed Re filament in 5 μl of a silica-gel/phosphoric acid mixture (Gerstenberger and Haase, 1997), and U and Pb isotopic measurements made on a GV Isoprobe-T multicollector thermal ionization mass spectrometer equipped with an ion-counting Daly detector. Pb isotopes were measured by peak-jumping all isotopes on the Daly detector for 160 cycles, and corrected for 0.16 ± 0.03%/a.m.u. (1 sigma error) mass fractionation. Transitory isobaric interferences due to high-molecular weight organics, particularly on ^{204}Pb and ^{207}Pb, disappeared within approximately 30 cycles, while ionization efficiency averaged 10^4 cps/pg of each Pb isotope. Linearity (to $\geq 1.4 \times 10^6$ cps) and the associated deadtime correction of the Daly detector were determined by analysis of NBS982. Uranium was analysed as UO_2^+ ions in static Faraday mode on 10^{12} Ω resistors for 300 cycles, and corrected for isobaric interference of $^{233}U^{18}O^{16}O$ on $^{235}U^{16}O^{16}O$ with an $^{18}O/^{16}O$ of 0.00206. Ionization efficiency averaged 20 mV/ng of each U isotope. U mass fractionation was corrected using the known $^{233}U/^{235}U$ ratio of the EARTHTIME tracer solution.

CA-TIMS U–Pb dates and uncertainties were calculated using the algorithms of Schmitz and Schoene (2007), EARTHTIME ET535 tracer solution (Condon et al., 2015) with calibration of $^{235}U/^{205}Pb$ = 100.233, $^{233}U/^{235}U$ = 0.99506, and $^{205}Pb/^{204}Pb$ = 11268, and U decay constants recommended by Jaffey et al. (1971) and $^{238}U/^{235}U$ of 137.818 from (Hiess et al., 2012). $^{206}Pb/^{238}U$ ratios and dates were corrected for initial ^{230}Th disequilibrium using $D_{Th/U} = 0.20 \pm 0.05$ (1s) and the algorithms of Crowley et al. (2007), resulting in an increase in the $^{206}Pb/^{238}U$ dates of 0.09 Ma. All common Pb in analyses was attributed to laboratory blank and subtracted based on the measured laboratory Pb isotopic composition and associated uncertainty. U blanks are estimated at 0.013 ± 0.009 pg (1s).

A weighted mean $^{206}Pb/^{238}U$ date was calculated from equivalent dates (probability of fit >0.05) using Isoplot 3.0 (Ludwig, 2003, 2009). Error on the weighted mean date is given as ± x/y/z, where x

Table 1
Three grains from lowermost Naturita were analysed. Grains 15, 45, and 50 yielded dates of 96.12 ± 0.10, 95.64 ± 0.11, and 104.67 ± 0.13 Ma, respectively. Four grains from Deep Eddy were analysed. Grains 1, 11, 103, and 125 yielded dates of 99.68 ± 0.14, 100.59 ± 0.09, 99.82 ± 0.22 Ma, and 100.72 ± 0.12 Ma, respectively. The two youngest dates yielded a weighted mean of 99.72 ± 0.12/0.12/0.16 Ma (MSWD = 1.1, probability of fit = 0.30). CA-TIMS zircon U–Pb isotopic data.

Sample							Radiogenic Isotope Ratios								Isotopic Dates					
	$\frac{Th}{U}$	$^{206}Pb^*$ $\times 10^{-13}$ mol	mol % $^{206}Pb^*$	$\frac{Pb^*}{Pb_c}$	Pb_c (pg)	$\frac{^{206}Pb}{^{204}Pb}$	$\frac{^{208}Pb}{^{206}Pb}$	$\frac{^{207}Pb}{^{206}Pb}$	% err	$\frac{^{207}Pb}{^{235}U}$	% err	$\frac{^{206}Pb}{^{238}U}$	% err	corr. coef.	$\frac{^{207}Pb}{^{206}Pb}$	±	$\frac{^{207}Pb}{^{235}U}$	±	$\frac{^{206}Pb}{^{238}U}$	±
(a)	(b)	(c)	(c)	(c)	(c)	(d)	(e)	(e)	(f)	(e)	(f)	(e)	(f)		(g)	(f)	(g)	(f)	(g)	(f)
Naturita-Mussentuchit																				
z1	0.351	0,2425	97.84%	13	0.44	842	0.112	0,048187	1208	0,099767	1289	0,015023	0.109	0772	107.39	28.51	96.56	1.19	96.12	0.10
z2	0.672	0,1610	97.70%	13	0.31	787	0.215	0,048611	1382	0,100132	1475	0,014946	0.117	0812	128.06	32.50	96.90	1.36	95.64	0.11
z3	0.252	0,1530	97.39%	11	0.34	693	0.081	0,048185	1564	0,108703	1668	0,016369	0.123	0866	107.30	36.93	104.78	1.66	104.67	0.13
Deep Eddy																				
z1	0.546	0,1276	97.74%	13	0.24	801	0.175	0,047831	1398	0,103807	1491	0,015748	0.118	0806	89.83	33.12	100.28	1.42	100.72	0.12
z2	0.681	0,0521	95.25%	6	0.21	381	0.218	0,048874	2979	0,105112	3169	0,015605	0.223	0859	140.75	69.92	101.48	3.06	99.82	0.22
z3	0.471	0,1554	98.40%	18	0.21	1133	0.151	0,047808	0.976	0,103616	1045	0,015726	0.095	0747	88.71	23.13	100.11	1.00	100.59	0.09
z4	0.795	0,1145	96.71%	10	0.32	550	0.254	0,047602	2027	0,102236	2158	0,015584	0.145	0914	78.49	48.11	98.84	2.03	99.68	0.14

(a) z1, z2, etc. are labels for analyses composed of single zircon grains that were annealed and chemically abraded (Mattinson, 2005). Labels in bold denote analyses used in weighted mean calculations.
(b) Model Th/U ratio calculated from radiogenic 208Pb/206 Pb ratio and 207 Pb/235U date.
(c) Pb* and Pbc are radiogenic and common Pb, respectively. mol % $^{206}Pb^*$ is with respect to radiogenic and blank Pb.
(d) Measured ratio corrected for spike and fractionation only. Fractionation correction is 0.16 ± 0.03 (1 sigma) %/amu (atomic mass unit) for single-collector Daly analyses, based on analysis of EARTHTIME 202 Pb–205Pb tracer solution.
(e) Corrected for fractionation and spike. Common Pb in zircon analyses is assigned to procedural blank with composition of 206Pb/204 Pb = 18.12 ± 1.67%; 207Pb/204 Pb = 15.45 ± 1.19%; 208Pb/204 Pb = 37.51 ± 1.47% (1 sigma). 206 Pb/238U and 207Pb/206 Pb ratios corrected for initial disequilibrium in 230Th/238U using a D(Th/U) of 0.20 ± 0.05 (1 sigma).
(f) Errors are 2 sigma, propagated using algorithms of Schmitz and Schoene (2007) and Crowley et al. (2007).
(g) Calculations based on the decay constants of Jaffey et al. (1971). 206 Pb/238U and 207Pb/206 Pb dates corrected for initial disequilibrium in 230Th/238U using a D(Th/U) of 0.20 ± 0.05 (1 sigma).

is the internal error based on analytical uncertainties only, including counting statistics, subtraction of tracer solution, and blank and initial common Pb subtraction, y includes the tracer calibration uncertainty propagated in quadrature, and z includes the ^{238}U decay constant uncertainty propagated in quadrature. Internal error should be considered when comparing our date with ^{206}Pb/^{238}U dates from other laboratories that used the same EARTHTIME tracer solution or a tracer solution that was cross-calibrated using EARTHTIME gravimetric standards. Error including the uncertainty in the tracer calibration should be considered when comparing our date with those derived from other geochronological methods using the U–Pb decay scheme (e.g., LA-ICP-MS). Error including uncertainties in the tracer calibration and ^{238}U decay constant (Jaffey et al., 1971) should be considered when comparing our date with those derived from other decay schemes (e.g., ^{40}Ar/^{39}Ar, ^{187}Re-^{187}Os). Errors for weighted mean date and errors on dates from individual grains are given at 2s.

3.3. Maximum depositional age

Assessing the MDA of each grain and each sample utilized within this study consisted of processing the data via seven different methodologies (see Coutts et al., 2019; Dickinson and Gehrels, 2009a, 2009b; Johnston et al., 2009; Lawton and Bradford, 2011), including 1) youngest single grain age (YSG); 2) youngest graphical detrital zircon age (YPP); 3) youngest detrital zircon age (YDZ); 4) the weighted mean average age (YC1σ) (+3); 5) Weighted Average; 6) weighted mean average age (YC2σ) (+3); and 7) TuffZirc (Zircon Age Extractor) (+6) as in Tucker et al. (2013, 2016, and references therein). A number of studies have pointed out potential biases of research involving detrital zircon geochronological data (e.g. hydrological sorting, transport variability or climate) (Hietpas et al., 2011; Lawrence et al., 2011; Tucker et al., 2013). Noted biases mostly affect provenance-based detrital zircons studies, and have little bearing on studies focused on maximum depositional age reconstruction; however, the latter can also be subject to error. To mitigate error in the calculation of grain age(s) and MDA, we conducted multiple sampling of grains and used CL imaging to identify morphology, grain irregularities or cores following Corfu et al. (2003).

3.4. Contemporaneity of volcanism and sedimentation

Recent studies have taken significant steps to better understand the variables influencing the emplacement of volcaniclastic and volcanilithic detritus into the sedimentological record. This particular interest is due to their ever-increasing utility to derive absolute and maximum depositional ages (MDAs) via various geochronological methods (Amidon et al., 2005a,b; Roberts, 2007; Dickinson and Gehrels, 2009a, 2009b; Thomas, 2011, Zimmermann et al., 2018; D'Emic et al., 2019, Rossignol et al., 2019). Although this is far from resolved, meaningful linkages between a volcanic source terrane and emplacement into the rock record are beginning to strengthen. Recent work by Rossignol et al. (2019) made significant advances to better constrain synchronicity between volcanism and sedimentation (mainly volcaniclastics). In order to achieve this, Rossignol et al. (2019) put forth the following guidelines: 1) samples must be recovered from volcaniclastic sediment; 2) reproducible data; 3) the vertical sequence of sampled strata must become progressively younger upsection; 4) the grains are preferably autocrysts (within tens to hundreds kyr or less before eruption), with key morphological characteristics (euhedral), free of inclusions and not suffering from Pb loss. If achieved, Rossignol et al. (2019) presented substantial support for this concept for volcaniclastics, and by translation, the same concept should aid in more rigorously assessing possible MDAs for volcanilithic-rich units (secondary deposits).

Therefore, we clearly define that zircons utilized within this facet of the study are older than that of the real sedimentation age and are autocrystic in nature (assuming that the system remains somewhat closed and the grains that incurred significant Pb loss were omitted). Thus, this study parallels Rossignol et al. (2019), in that we identify the volcanilithic unit, the maximum depositional age, and its uncertainty to identify near-coeval and non-coeval (reworked) volcanic detritus emplacement into the Mussentuchit Wash depo-centre. However, zircon separates for this study were collected from volcanilithic-rich units rather than volcaniclastic units; therefore, they inherently experienced reworking, transport, and minimal multi-phased depositional histories (Cifelli et al., 1997; Garrison et al., 2007; Kirkland et al., 2016; and this study). To account for this, we apply the most accepted methods for determining MDAs based on the rigorous method reviews conducted by Coutts et al. (2019). For datasets containing between 50 and 120 individual grains, YSG and YDZ are the most appropriate (Coutts et al., 2019; Dickinson and Gehrels, 2009a, 2009b; Finzel, 2017; May et al., 2013; Wotzlaw et al., 2014, pg 12; D'Emic et al., 2019; Rossignol et al., 2019). Yet, this study holds to the definition put forth by Rossignol et al. (2019) in that the youngest zircon population (maximum depositional age [MDA]) must be identified by multiple zircon grains that are representative of the eruption age, prior to the inclusion in a volcaniclastic or sedimentary (volcanilithic-rich) sedimentary rock. Therefore, we consider YDZ ($n = 3$) and its uncertainties as a more conservative determination of MDA.

To secondarily assess both the MDAs and contemporaneity of volcanism and sedimentation, this study employed the Kolmogorov-Smirnov test (K–S test). The K–S test is a nonparametric method for comparing cumulative probability distributions (DeGraaff-Surpless et al., 2003; Barbeau et al., 2009; Guynn and Gehrels, 2010; Tucker et a., 2016). This study utilized the cumulative distribution functions (CDFs) based on ages and their uncertainties and excluded those that failed this test. For p-values <0.05, the two sets of grain-age data could not have been derived from the same-aged source, whereas for p-values >0.05, the differences between the two samples may be due to random selection from the same-aged source (Barbeau et al., 2009). All data presented is based on the KS-p values using error in the CDF, and herein reported as “p-values”.

4. Results

4.1. Detrital zircon age clusters via LA-ICP-MS

Zircon grains ranged from well-rounded and abraded to well-preserved euhedral grains. Individual grains predominantly reflect varying degrees of complex zonations, yet a few reflect patchy zoning or even metamorphic textures. Zonations commonly exhibit simple bimodal to growth zoning, with many preserving distinct cores. Individual grains exhibit a wide variety of detrital characteristics, including cracks, fissures, fractures, and rounded terminal-ends. Samples collected from the uppermost Buckhorn Conglomerate, uppermost Ruby Ranch, and Lindsay's Site contain above-average detrital characteristics; whereas, the remainder of the samples tend to preserve more euhedral grains. Cretaceous aged grains lack metamorphic zonations (antecrysts) along the exterior rims; therefore, these grains have been identified as igneous zonations typical of autocrysts, lowering the chance of reset ages being ablated. All samples and their respective site descriptions are detailed in Online Supplement A, and all LA-ICP-MS data is presented within Online Supplementary tables 1A-1K.

4.1.1. Uppermost Buckhorn Conglomerate

One hundred and eleven grains were recovered and analysed (107 reported), yielding multiple Mesozoic age populations for roughly half of the grains (±49.5%), with the remainder from Paleozoic (19.6%) and Pre-Cambrian (30.8%) sources. Lower Cretaceous grains represented the majority of Mesozoic grains (90.6%). Analysis of the sample yielded the following youngest age signatures: YSG at 115 (±2.9) Ma; YPP at 115.2 Ma; YDZ at 115.1 + 2.3–3.3 Ma; YC1σ (±3) at 115.0 (±1.8) Ma; Weighted Average (3) at 117.2 ± 2.5 Ma; YC2σ (+3) at 115.0 (±2.9) Ma; TuffZirc (6) age at 117.6 + 2.7–2.5 Ma (Fig.5a, Table 2). The mean of the youngest age signatures is ±115.7 Ma, placing it in the late Aptian (Table 2; Supplementary Table 1A) (see Fig. 5a).

4.1.2. Uppermost Ruby Ranch

Ninety-five grains were recovered and analysed (76 reported), yielding multiple Mesozoic age populations for the vast majority (±81.5%), with the remainder from Paleozoic (5.2%) and Pre-Cambrian (13.2%) sources. Lower Cretaceous grains are the only representative Mesozoic grains (100%) present. Analysis of the sample yielded the following youngest age signatures: YSG at 108.0 (±2.0) Ma; YPP at 109.1 Ma; YDZ at 107.7 + 2.8–4.2 Ma; YC1σ (+3) at 111.2 (±1.5) Ma; Weighted Average (3) at 110.1 ± 4.5 Ma; YC2σ (+3) at 110.1 (±2.1) Ma; TuffZirc (6) age at 112.8 + 0.4–1.0 Ma (Fig. 5a, Table 2). The mean of the youngest age signatures is ±109.9 Ma (Table 2; Supplementary Table 1B).

4.1.3. Middle Mussentuchit

Seventy-six grains were recovered and analysed (45 reported), yielding multiple age populations with (±31.1%) of the sample represented by Mesozoic aged grains and the remainder from Paleozoic (35.5%) and Pre-Cambrian (33.3%) sources. Lower Cretaceous grains represent only 21% of the overwhelmingly Upper

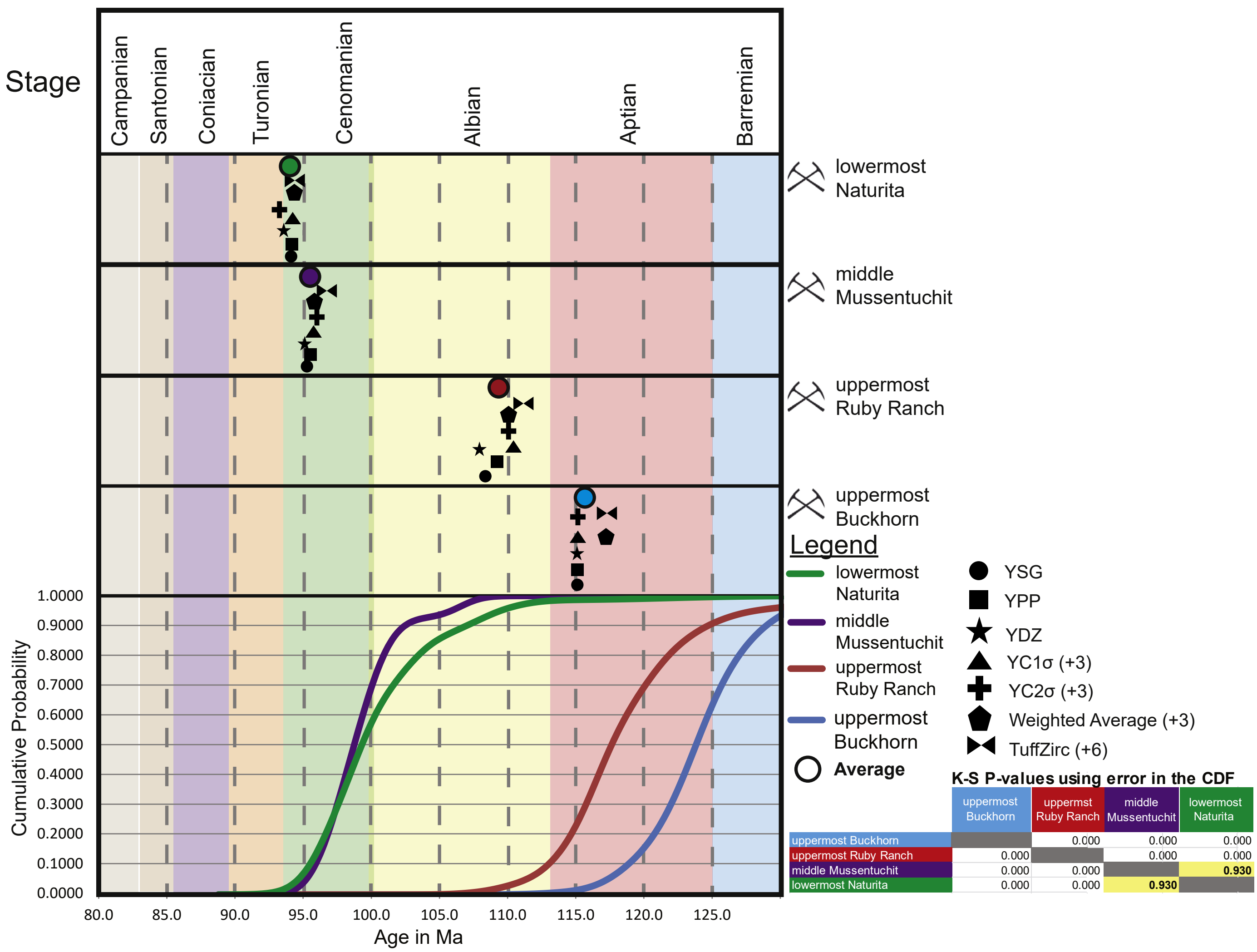

Fig. 5. a: Temporal relationship of the seven metrics (YSG, YPP, YDZ, YC1σ (+3), Weighted Average, YC2σ (+3), and TuffZirc (+6)) utilized within this study, of the four stratigraphically key populations (uppermost Buckhorn Conglomerate, uppermost Ruby Ranch, medial Mussentuchit, and lowermost Naturita, along with and the youngest combined population). Also displayed if the K–S Test and CDF's to show the weak genetic relationship across the samples stratigraphic section in the Cedar Mountain Formation. Age placement based on Cohen et al. (2013); v2019/05. Figure 6b: Temporal relationship of the seven metrics (YSG, YPP, YDZ, YC1σ (+3), Weighted Average, YC2σ (+3), and TuffZirc (+6)) utilized within this study, of the seven sampled populations based at key fossil sites (Fortunate Son, Stormy Theropod, SLF, Deep Eddy, Suicide Hill, Mini Troll, and Lindsay's Site, along with and the youngest combined population). Also displayed is the K–S Test and CDF's to show the weak genetic relationship between lower and upper stratigraphic section in the Mussentuchit Member. Age placement based on Cohen et al. (2013); v2019/05.

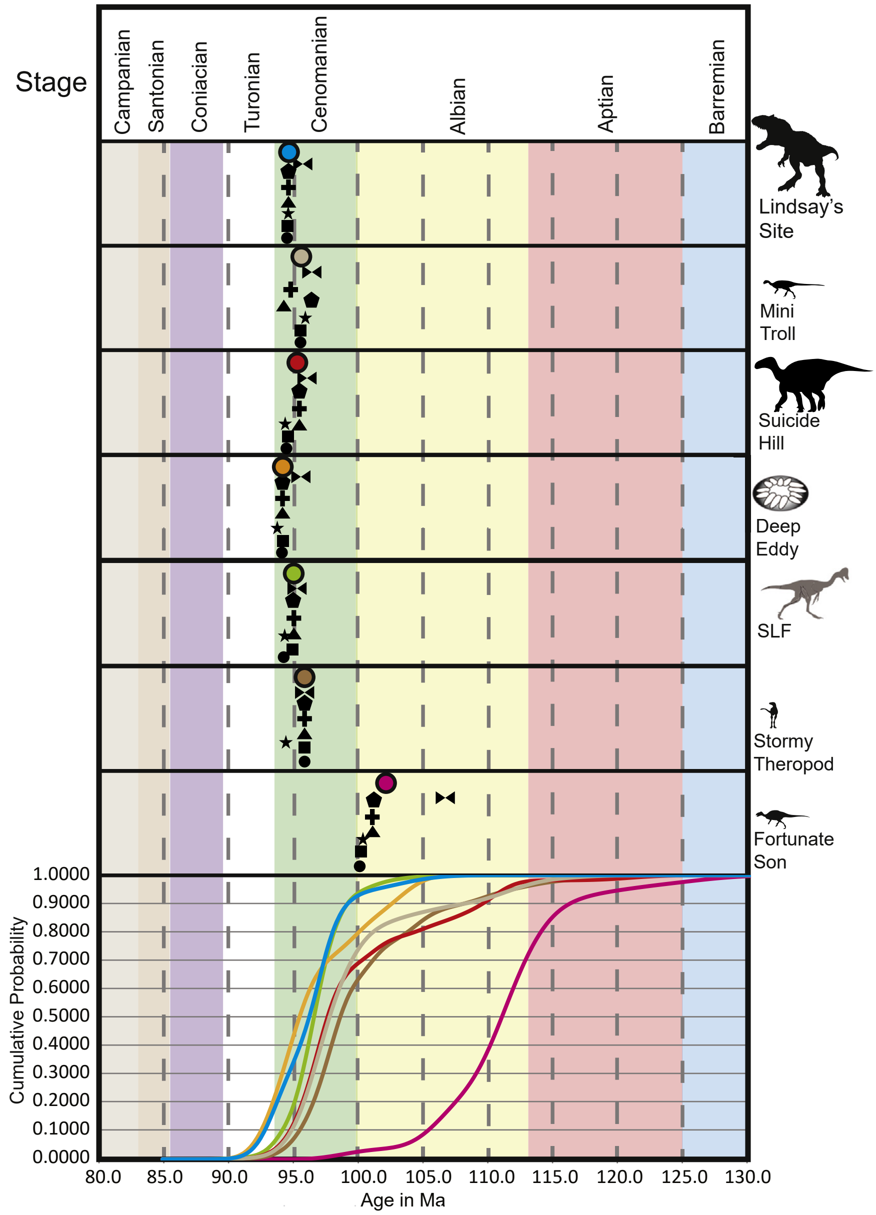

K-S P-values using error in the CDF

	Fortunate Son	Stormy Theropod	SLF	Deep Eddy	Suicide Hill	Mini Troll	Lindsay's Site
Fortunate Son		0.000	0.000	0.000	0.000	0.000	0.000
Stormy Theropod	0.000		0.000	0.028	**0.502**	**0.516**	0.031
SLF	0.000	0.000		**0.457**	0.027	0.004	**0.878**
Deep Eddy	0.000	0.028	**0.457**		**0.172**	**0.106**	**0.998**
Suicide Hill	0.000	**0.502**	0.027	**0.172**		**0.994**	**0.404**
Mini Troll	0.000	**0.516**	0.004	**0.106**	**0.994**		**0.247**
Lindsay's Site	0.000	0.031	**0.878**	**0.998**	**0.404**	**0.247**	

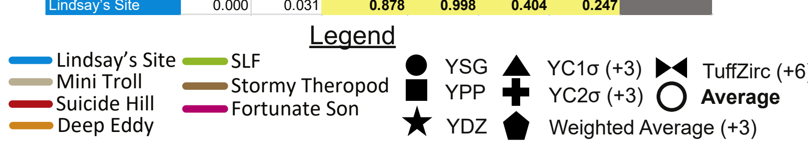

Fig. 5. (*continued*).

Cretaceous distribution with most grains within the Cenomanian. Analysis of the sample yielded the following youngest age signatures: YSG at 96.1 (±1.3) Ma; YPP at 96.7 Ma; YDZ at 95.8 at+1.0−1.3 Ma; YC1σ (+3) at 96.5 (±1.3) Ma; Weighted Average (3) at 96.5 (±1.3) Ma; YC2σ (+3) at 96.5 (±1.9) Ma; TuffZirc (6) age at 97.3 (+0.8−1.2) Ma (Fig. 5a, Table 2). Emplacement of middle Mussentuchit Member sediments occurred no later than ±96.5 Ma (Table 2; Supplementary Table 1C).

4.1.4. Lowermost Naturita

One hundred and thirty-five grains were recovered and analysed (126 reported), yielding multiple age populations. A large

Table 2
Comparison of different metrics utilised within this study to interpret the Maximum Depositional Age (MDAs) for each detrital Samples (Modified from Tucker et al., 2016). Note: These include: (1) YSG of all 11 samples presented with ±1σ errors; (2) YPP or the graphical age based on a histogram derived from Isoplot; (3) YDZ of all 11 populations with the age range (+or −), and the confidence of that metric; (4) YC1σ (+3) of all 11 samples presented with the final age, weighted mean average, systematic error, and mean square of weighted deviates (MSWD) at a ±1σ error; (5) weighted average of all 11 populations with the age, confidence, amount of grains rejected, MSWD, and the overall probability; (6) YC2σ (+3) of all 10 samples with the final age, weighted mean, systematic error, and MSDW at a ±2σ error; (7) TuffZirc (+6) presented with the final age, confidence, and the group size; and (8) average of the results from all seven maximum depositional age calculation approaches.

Analysis		Uppermost Buckhorn	Uppermost Ruby Ranch	middle Mussentuchit	Lowermost Naturita	Fortunate Son	Stormy Theropod	SLF	Deep Eddy	Suicide Hill	Mini Troll	Lindsay's Site
YSG	Age	115	108.0	96.1	94.3	100.1	96.2	94.9	94.2	94.6	95.7	94.3
	Error (±2σ)	±2.9	±2.0	±1.3	±1.1	±1.5	±2.6	±0.9	±1.5	±1.7	±2.4	±1.5
YPP	Age	115.2	109.1	96.7	94.2	100.6	96.8	95.0	94.6	94.9	95.9	94.1
YDZ	Age	115.1	107.7	95.8	93.9	100.1	94.8	94.7	93.7	94.6	95.4	94.1
	Range	+2.3/-3.3	+2.8/-4.2	+1.0/-1.3	+1.8/-1.8	+1.6/-1.7	+1.0/-2.6	+0.6/-1.2	+1.3/-1.3	+1.3/-1.9	+1.1/-2.5	+0.8/-1.0
	Confidence	95%	95%	95%	95%	95%	95%	95%	95%	95%	95%	95%
YC1σ (+3)	Final Age	115.0 ± 1.8 (1.6%)	111.2 ± 1.5 (1.4%)	96.5 ± 1.3 (1.4%)	94.5 ± 1.3 (1.4%)	101.6 ± 1.5 (1.4%)	96.6 ± 1.6 (1.7%)	95.1 ± 1.2 (1.3%)	94.5 ± 1.4 (1.5%)	95.6 ± 1.4 (1.5%)	94.6 ± 2.0 (2.2%)	94.7 ± 1.3 (1.4%)
	Weighted Mean Age	115.0 ± 1.3 (1.1%)	110.1 ± 0.9 (0.8%)	96.5 ± 0.8 (0.8%)	94.5 ± 0.7 (0.8%)	101.6 ± 1.0 (0.9%)	96.6 ± 1.1 (1.2%)	95.1 ± 0.7 (0.7%)	94.5 ± 0.9 (1.0%)	95.6 ± 0.9 (1.0%)	94.6 ± 1.8 (1.9%)	94.7 ± 0.8 (0.9%)
	Systematic Error	1.1%	1.1%	1.1%	1.1%	1.1%	1.1%	1.1%	1.1%	1.1%	1.1%	1.1%
	MSWD	5.8	5.5	1.0	2.0	3.4	0.1	0.2	0.2	0.9	0.2	0.8
WEIGHTED AVERAGE (+3)	Age	117.2 (±2.5)	110.1 (±4.5)	96.5 (±0.75)	93.5 (±0.7)	101.6 (±3.8)	96.6 (±1.1)	95.1 (±0.7)	94.5 (±0.9)	95.6 (±0.9)	96.2 (±0.8)	94.7 (±0.8)
	Confidence	95.0%	95.0%	95.0%	95.0%	95.0%	95.0%	95.0%	95.0%	95.0%	95.0%	95.0%
	Rejection	0	0	0	0	0	0	0	0	0	0	0
	MSWD	1.2	5.5	0.97	2.8	3.4	1.2	0.23	0.2	0.94	0.08	0.76
	Probability	0.30	0.00	0.38	0.06	0.04	0.069	0.80	0.82	0.39	0.93	0.47
YC2σ (+3)	Final Age	115.0 ± 2.9 (2.5%)	110.1 ± 2.1 (2.0%)	96.5 ± 1.9 (1.9%)	94.5 ± 1.8 (1.9%)	101.6 ± 2.2 (2.2%)	96.6 ± 2.5 (2.6%)	95.1 ± 1.7 (1.8%)	94.5 ± 2.1 (2.2%)	95.6 ± 2.1 (2.2%)	94.6 ± 3.7 (3.9%)	94.7 ± 2.0 (2.1%)
	Weighted Mean Age	115.0 ± 2.6 (2.3%)	110.1 ± 1.8 (1.6%)	96.5 ± 1.5 (1.6%)	94.5 ± 1.5 (1.6%)	101.6 ± 1.9 (1.9%)	96.6 ± 2.3 (2.4%)	95.1 ± 1.4 (1.4%)	94.5 ± 1.9 (2.0%)	95.6 ± 1.9 (1.9%)	94.6 ± 3.5 (3.7%)	94.7 ± 1.7 (1.8%)
	Systematic Error	1.1%	1.1%	1.1%	1.1%	1.1%	1.1%	1.1%	1.1%	1.1%	1.1%	1.1%
	MSWD	1.5	1.4	0.2	0.1	0.8	0.0	0.1	0.1	0.2	0.0	0.2
TUFF ZIRC (+6)	Age	117.6 +2.7/-2.5	112.8 +0.4/-1.0	97.3 +0.8/-1.2	94.9 +0.5/-0.6	108.9 +0.1/-1.5	96.8 +0.5/-0.6	95.5 +0.8/-0.5	95.3 +1.68/-1.1	96.3 +0.8/-1.7	96.5 +0.6/-0.8	95.3 +2.8/-1.2
	Confidence	93.8%	87.8%	96.9%	96.9%	75%	96.9%	96.9%	96.9%	96.9%	96.9%	96.9%
	Group Size	5 of 6	4 of 6	6 of 6	6 of 6	3 of 6	6 of 6	6 of 6	6 of 6	6 of 6	6 of 6	6 of 6
Average		**115.7 Ma**	**109.9 Ma**	**96.5 Ma**	**94.2 Ma**	**102.1 Ma**	**96.4 Ma**	**95.1 Ma**	**94.5 Ma**	**95.3 Ma**	**95.6 Ma**	**94.6 Ma**

percentage (68.4%) of the sample is represented by Mesozoic-aged grains (with just over half within the Upper Cretaceous), with the remainder from Paleozoic (11%) and Pre-Cambrian (20.6%) sources. Analysis of the sample yielded the following youngest age signatures: YSG at 94.3 (±1.1) Ma; YPP at 94.2 Ma; YDZ at 93.9 at +1.8−1.8 Ma; YC1σ (+3) at 94.5 (±1.3) Ma; Weighted Average (3) at 93.5 (±0.7) Ma; YC2σ (+3) at 94.5 (±1.8) Ma; TuffZirc (6) age at 94.9 (+0.5−0.6) Ma (Fig. 5a, Table 2). Emplacement of lowermost Naturita sediments occurred no later than ±94.2 Ma (Table 2; Supplementary Table 1D).

Fossil-site Samples were collected throughout the study area with fresh sediment collected from rock that directly entombed the fossil assemblage. Details on the taxonomic identity of the specific fossil assemblage are provided in Online Supplement A.

4.1.5. Fortunate Son

One hundred and twenty-five grains were recovered and analysed (109 reported), yielding multiple age populations, with over half (77.9%) of the sample represented by Mesozoic aged grains (with 97.6% in the Lower Cretaceous), and the remainder from Paleozoic (8%) and Pre-Cambrian (15%) sources. Analysis of the sample yielded the following youngest age signatures: YSG at 100.1 (±1.5) Ma; YPP at 100.6 Ma; YDZ at 100.1 + 1.6−1.7 Ma; YC1σ (+3) at 101.6 (±1.5) Ma; Weighted Average (3) at 101.6 ± 3.8 Ma; YC2σ (+3) at 101.6 (±2.2) Ma; TuffZirc (6) age at 108.9 + 0.1−1.5 Ma (Fig. 5b, Table 2). Burial of fossil remains and preserving sediments occurred no later than 102.1 Ma (Table 2; Supplementary Table 1E).

4.1.6. Stormy Theropod

One hundred and twenty grains were recovered and analysed (109 reported), yielding multiple age populations. Over half (±66%) of the sample represented by Mesozoic aged grains, with the remainder from Paleozoic (9%) and Pre-Cambrian (25%) sources. Cretaceous grains represent an overwhelming majority (65%) of the Mesozoic populations. Analysis of the sample yielded the following youngest age signatures: YSG at 96.2 (±2.6) Ma; YPP at 96.8 Ma; YDZ at 94.8 + 1.0−2.6 Ma; YC1σ (+3) at 96.6 (±1.6) Ma; Weighted Average (3) at 96.6 ± 1.1 Ma; YC2σ (+3) at 96.6 (±2.5) Ma; TuffZirc (6) age at 96.8 + 0.5−0.6 Ma (Fig. 5b, Table 2). Burial of the fossil by preserving sediments occurred no later than 96.4 Ma (Table 2; Supplementary Table 1F).

4.1.7. SLF

One hundred and six grains were recovered and analysed (101 reported), yielding multiple age populations, with nearly all (±95%) of the sample represented by Mesozoic aged grains, with the remainder from Paleozoic (2.0%) and Pre-Cambrian (3.0%) sources. Cretaceous grains represent all of the recovered Mesozoic grain ages, with an overwhelming mid-Cretaceous distribution of gain ages in the Cenomanian (82.7%) and the remainder within the Albian (17.2%). Analysis of the sample yielded the following youngest age signatures: YSG at 94.9 (±0.9) Ma; YPP at 95.0 Ma; YDZ at 94.7 +0 .6−1.2 Ma; YC1σ (+3) at 95.1 (±1.2) Ma; Weighted Average (3) at 95.1 ± 0.7 Ma; YC2σ (+3) at 95.1 (±1.7) Ma; TuffZirc (6) age at 95.5 + 0.08−0.57 Ma (Fig. 5b, Table 2). Emplacement of entombed partial skeleton remains and preserving sediments occurred no later than 95.1 Ma (Table 2; Supplementary Table 1G).

4.1.8. Deep Eddy

One hundred and thirty grains were recovered and analysed (93 reported), yielding multiple age populations, represented by Mesozoic aged grains (20.8%), with the remainder from the Paleozoic (28.6%) and Pre-Cambrian (51.6%) sources. Analysis of the sample yielded the following youngest age signatures: YSG at 94.2 (±1.5) Ma; YPP at 94.6 Ma; YDZ at 93.7 + 1.3−1.3 Ma; YC1σ (+3) at 94.5 (±1.4) Ma; Weighted Average (3) at 94.5 ± 0.9 Ma; YC2σ (+3) at 94.5 (±2.1) Ma; TuffZirc (6) age at 95.3 + 1.7−1.1 Ma (Fig. 5b, Table 2). Emplacement of entombed dinosaur egg remains and preserving sediments occurred no later than 94.5 Ma (Table 2; Supplementary Table 1H).

4.1.9. Suicide Hill

One hundred and sixteen grains were recovered and analysed (89 reported), yielding multiple age populations, with a large majority (65.2%) of the sample represented by Mesozoic aged grains (of that, 50.0% from the Upper Cretaceous), with a minor subset in the Palaeozoic (10.1%), and the remainder of grains in the Pre-Cambrian (24.7%) sources. Analysis of the sample yielded the following youngest age signatures: YSG at 94.6 (±1.7) Ma; YPP at 94.9 Ma; YDZ at 94.6 + 1.3−1.9 Ma; YC1σ (+3) at 95.6 (±1.4) Ma; Weighted Average (3) at 95.6 ± 0.9 Ma; YC2σ (+3) at 95.6 (±2.1) Ma; TuffZirc (6) age at 96.3 + 0.8−1.7 Ma (Fig. 5b, Table 2). Emplacement of fossil remains and preserving sediments occurred no later than 95.3 Ma (Table 2; Supplementary Table 1I).

4.1.10. Mini Troll

One hundred and twenty-nine grains were recovered and analysed (121 reported), yielding multiple age populations, with nearly all (±92%) of the sample represented by Mesozoic aged grains, and the remainder represented by Palaeozoic (4%) and Pre-Cambrian (4%) sources. Upper Cretaceous grains are only represented by a minor subset (3.1%); whereas mid-Cretaceous Cenomanian grains represent a majority (84.6%). Analysis of the sample yielded the following youngest age signatures: YSG at 95.7 (±2.4) Ma; YPP at 95.9 Ma; YDZ at 95.4 + 1.1−2.5 Ma; YC1σ (+3) at 94.6 (±2.0) Ma; Weighted Average (3) at 96.2 ± 0.8 Ma; YC2σ (+3) at 94.6 (±3.7) Ma; TuffZirc (6) age at 96.5 + 0.6−0.8 Ma (Fig. 5b, Table 2). Emplacement of entombed fossil remains and preserving sediments occurred no later than 95.6 Ma (Table 2; Supplementary Table 1J).

4.1.11. Lindsay's site

Seventy-two grains were recovered and analysed (57 reported), yielding multiple age populations, though this sample presents atypical age distributions when compared to the rest. A smaller portion of the grains were (±31.5%) of the sample represented by Mesozoic aged grains (of that, 88% are within the lowermost Upper Cretaceous), with the remainder represented by Palaeozoic (7.0%) and the largest subset represented by Pre-Cambrian (61.4%) sources. Analysis of the sample yielded the following youngest age signatures: YSG at 94.3 (±1.5) Ma; YPP at 94.1 Ma; YDZ at 94.1 + 0.8−1.0 Ma; YC1σ (+3) at 94.7 (±1.3) Ma; Weighted Average (3) at 94.7 ± 0.8 Ma; YC2σ (+3) at 94.9 (±2.0) Ma; TuffZirc (6) age at 95.3 + 2.8−1.2 Ma (Fig. 5b, Table 2). Emplacement of entombed *Siats meekerorum* and associated other vertebrate remains and preserving sediments occurred no later than 94.6 Ma (Table 2; Supplementary Table 1J).

4.2. Detrital zircon age clusters

Several distinct age clusters are readily apparent in a combined probability density plot for all eleven (11) samples and are discussed herein (Fig. 6). Overall, for most samples, Mesozoic grain ages were measured for a majority of the recovered zircons; save for Lindsay's Site, which contains an atypical amount of Pre-Cambrian grains. Again, populations are based on a three-grain minimum (N > 3), and grain age and error is presented at 2 theta. A well-documented tectonic history and a well-formed backbone of prior work (Dickinson and Gehrels, 2003; DeCelles, 2004; Dickinson and Gehrels, 2009a,b; Willis, 1999; Laskowski et al.,

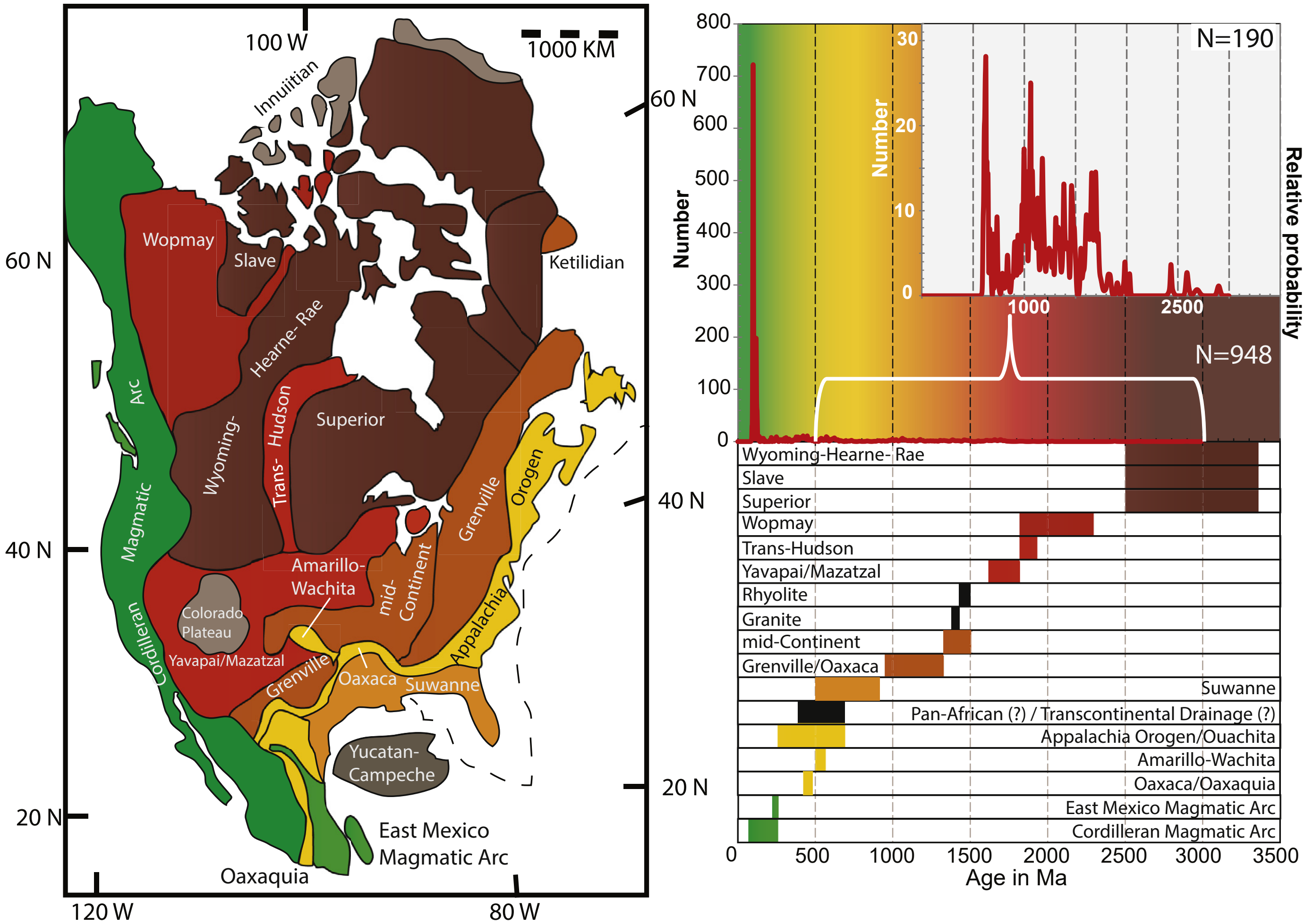

Fig. 6. Combined possible crustal provenances and age-distribution curve for all recovered detrital zircons from the Cedar Mountain Formation samples from the Mussentuchit Wash. North American map displaying the likely crustal provenances for each major detrital zircon age population reworked within the Cordilleran retroarc foreland basin system. Successive zircon age populations are shown below the age-distribution curve, is displayed with colour corresponding to the select crustal provinces. Modified and adapted from Dickenson and Gehrels (2009) and Laskowski et al. (2013); and references therein. Age placement based on Cohen et al. (2013); v2019/05. (For interpretation of the references to colour in this figure legend, the reader is referred to the Web version of this article.)

2013; and references therein), allows for a highly-detailed and well-supported interpretation of likely source terranes for major population within the recovered zircon data. As a whole, detrital zircon age spectra along with a probability density plot strongly reflect a collisional, Foreland Basin as identified by Cawood et al. (2012; pg876, Fig1D).

4.2.1. *Precambrian*

Samples are completely void of Archean-aged grains or populations, and contain only a minor handful of pre-Rhyacian Paleoproterozoic grains ages (>2.0 Ga) that have been linked to recycled continental fragments (Hoffman, 1988; Laskowski et al., 2013). Another possible source for extensively transported grains between 2.0 and 2.5 Ga is the Peace River Arch region; however, as suggested by Gehrels et al. (1995) and subsequent work by Linde et al. (2016), the inclusion of these grains rest on probable linked longshore transport. A larger proportion of Pre-Cambrian grains rest between 2.0 and 1.5 Ga, linked to the Trans-Hudson Orogeny, Wopmay, and undocumented terrane accretions and orogenic events (Fig. 6). Younger 1.7–1.0 Ga grains could be linked to the Yavapai, Mazatzal, and Grenville source terranes with associated accretionary or magmatic events across the accreting cratonic core (Gehrels et al., 1995; Van Schmus et al., 1996; Whitmeyer and Karlstorm, 2007). Likely sources due to proximity and paleocurrent drainages for Mesoproterozoic aged grains is the Mogollon Highlands to the southwest, and basement uplift and erosion via the westerly lying Sevier Orogenic Belt (reworking of Canyon Range, Pavant, Paxton Thrusting Phase detritus) in agreement with prior studies (Dickinson and Gehrels, 2008; Lawton and Bradford, 2011; Laskowski et al., 2013). A farther, but still possible, source for 1.7–1.95 Ga grains could be the Peace River Arch, along with other suggested far-flung source terranes that include, but are not limited to; 1) Antarctica; 2) Australia; 3) African; or even 4) proto-Rodinian supercontinent; yet, this remains unresolved (Fig. 6) (Gehrels et al., 1995; Laskowski et al., 2013; Linde et al., 2016). Minor Neoproterozoic populations in each of the samples are identified; however, within these, distinctive minor peaks are noted between 550 and 650 Myr, and have been linked to recycling of Appalachian, Grenville and possible Pan-African- Gondwana sources via transcontinental drainages and extensive continental-scale ergs (Dickenson and Gehrels, 2003; Laskowski et al., 2013).

4.2.2. *Phanerozoic-palaeozoic*

All samples contain grains and minor populations within the Paleozoic; however, they are minute (Fig. 6). Older Cambrian and Ordovician grain populations are more common in a majority of samples than those of Silurian to Permian age. Prior studies have linked many of these to both the Amarillo- Wichita uplift, later phase Appalachian Orogeny, along with continued reworking through the still long-lived erg's (Laskowski et al., 2013; and references therein).

4.2.3. Phanerozoic-mesozoic

Mesozoic-aged grains constitute over half (67%) of all recovered ages from the eleven (11) samples (670/991) (Figs. 6 and 7). Of these, an overwhelming majority lie within the Cretaceous (641/670), with only a few, sparse Triassic- or Jurassic-aged grains (29/670). Thus, early grains greatly reflect the ever-increasing and diverse heterogeneous nature of the Cordillera arc (DeCelles, 2004), all falling within Phases A, B, and a majority in C identified by DeCelles and Graham (2015) (Fig. 7). As with Proterozoic populations, recent literature allows for linkages to more-likely and less-likely source terranes across the Western Interior Basin. For recovered, and likely, recycled Triassic and Jurassic grain ages, sources possibly range from the Amarillo-Wichita uplift (300-200 Ma) and the Appalachian uplift, with many of the younger grain ages tied to westerly lying source terranes within the Cordilleran Arc (Dickinson and Gehrels, 2003, 2009a, 2009b, 2009a, 2009b; Laskowski et al., 2013; Gehrels and Pecha, 2014). Much of the regional correlations to potential source terranes rely on well-agreed upon Laurentian-margin orogenic systems along the southern Cordilleran margin (Gehrels and Pecha, 2014). Specific source terranes between 260 and 145 Myr include: 1) East Mexico Arc; 2) the Mojave Desert; 3) Wallowa/Olds Ferry Terrane; and early phases of the: 1) Western Coast Plutonic Complex; 2) Sierra Nevada Batholith; and 3) Omineca Belt (Gehrels et al., 2009; LaManskin et al., 2011; Gaschnig et al., 2017; Quinn et al., 2018) (Fig. 7).

Younger Mesozoic populations (Lower and Upper Cretaceous), can be readily linked to varied source terranes and sub-provinces within the then active Cordilleran Volcanic Arc (Gehrels et al., 2009). Based on the results of DeCelles and Graham (2015), the youngest populations can be directly linked to Phase A (160–140 Myr) and B (140–105 Myr), with the youngest being the medial portion of Phase C (105–80 Myr) of volcanism (Fig. 7) (DeCelles and Graham, 2015). Mirroring results of other regional studies, paleocurrent analysis within the Mussentuchit Wash indicates fluvio-deltaic flow orientations to the northeast (Dickinson and Gehrels, 2008; Suarez et al., 2012; and references therein). Therefore,

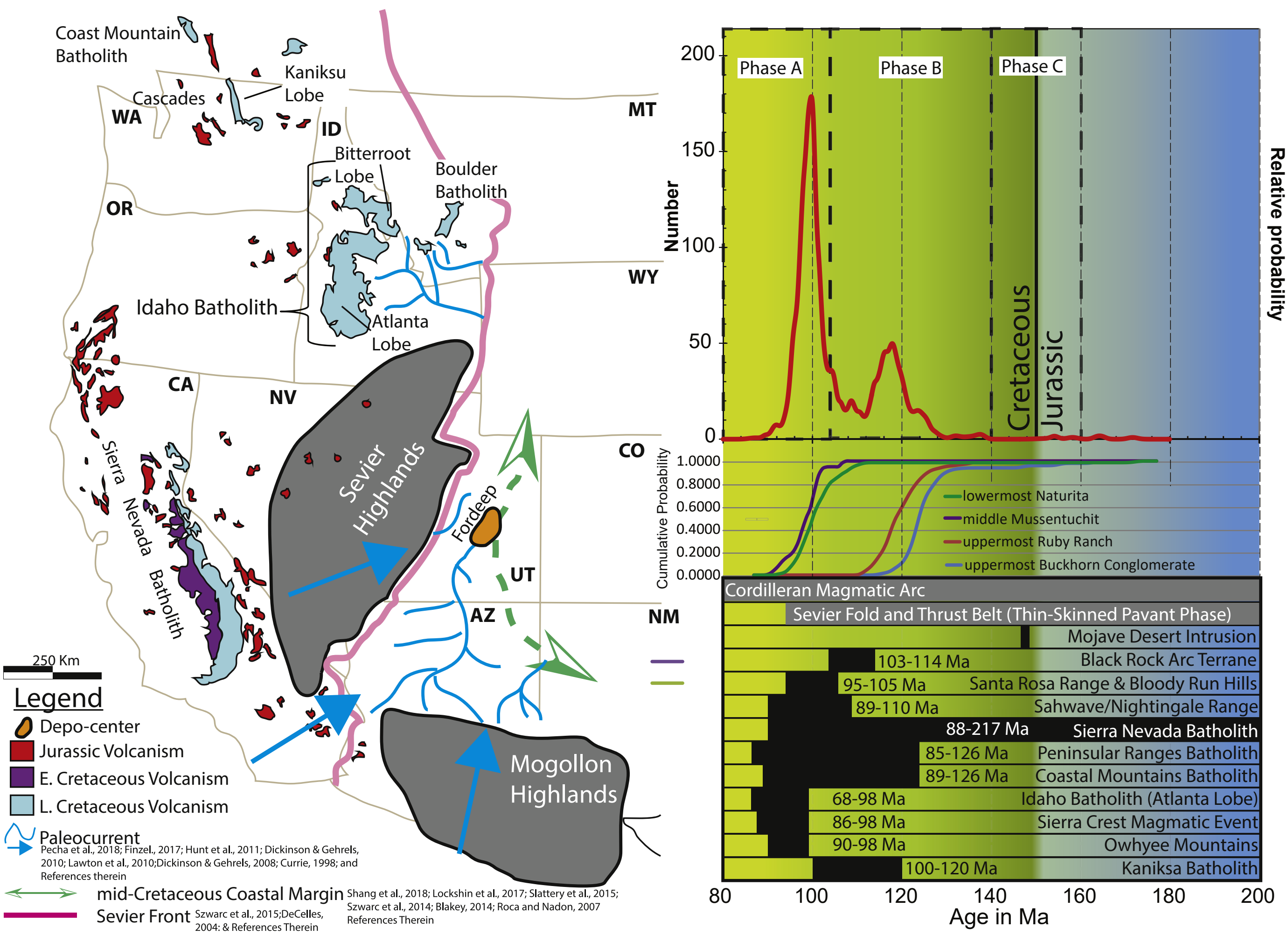

Fig. 7. Combined possible volcanic inliers within the westerly lying Cordilleran Arc and age-distribution curve for all recovered mid to upper Mesozoic detrital zircons from the Cedar Mountain Formation samples from the Mussentuchit Wash. North American map displaying both historically accepted and newly identified epiclastic and volcaniclastic/volcanilithic provenances for each major detrital zircon age population reworked within the Cordilleran retroarc foreland basin system. K–S Test and CDF's to show the weak genetic relationship between lower and upper stratigraphic section in the Mussentuchit Member, along with showing the distributions of zircons from Phases A, B and C originally described by DeCelles and Graham (2015) combined with likely inliers with synchronous phases of volcanic activity. Modified and adapted from Dickenson and Gehrels (2009); Gaschnig et al. (2009), 2010; Lawon et al. (2010); Hunt et al. (2011); Laskowski et al. (2013); DeCelles and Graham (2015); Linde et al. (2016); Sauer et al. (2017); Brown et al., 2018; and references therein. Age placement based on Cohen et al. (2013); v2019/05.

southwesterly lying source terranes within North American Cordillera are more likely contributors of younger zircons that are near-syndepositional in age (Dickinson and Gehrels, 2008; Lawton et al., 2010; Hunt et al., 2011; Laskowski et al., 2013; Szwarc et al., 2015; Brown et al., 2018; Pecha et al., 2018). Longer-lived tectonic events spanning the Early to Late Cretaceous (130–±90 Myr) that are also likely source terranes include the Northern Sierra Nevada, Central Sierra Nevada Batholith (Western Coast Plutonic Complex), and Peninsular Ranges Batholith. More localized tectonic events that could have also contributed zircons between 118 Ma and 92 Ma includes the Black Rock Arc Terrane, Sierra Crest Magmatic Event, Sahwave/Nightingale Range, Santa Rosa Range, Crowsnest, and the Bloody Run Hills (Brown et al., 2018) (Fig. 7). Recent investigations into the volcanic nature of the western lying arc indicate staggered periods volcanism of different inliers across the arc rather than a singular, long-lived event (Gaschnig et al., 2009; Finzel, 2017; Sauer et al., 2017; Brown et al., 2018; Quinn et al., 2018). Therefore, this study also considers more regional source terranes including the Owhyee Mountains, Atlanta Lobe of the Idaho Batholith and Eastern Coast Plutonic Complex (Fig. 7). Although these regional sources are geographically farther from our specific depo-centre, both air circulation models for the Cenomanian (flowing from the north-west to southeast-east), and the southerly oriented mass flow of Boreal water along the western margin of the Western Interior coastal margin, present plausible means of grain transport into our specific depo-centre (Hay and Floegel, 2012; Lowery et al., 2018). A variety of western lying source terranes (southwest, west, and northwest), along with a variety of transport systems, could be reason for variable temporal resolution across the Mussentuchit and the Cedar Mountain Formation as a whole (Fig. 7).

4.3. K–S provenance analysis

This study utilized the Kolmogorov-Smirnov test (K–S test) to evaluate the likelihood that the age profiles of zircons at sites are similar ($p > 0.05$; i.e. not statistically different) or dissimilar ($p < 0.05$). Statistically dissimilar samples suggest that the samples originated from different (possibly multiple) source terranes across the North American Craton; whereas, statistically similar samples argue for near-syndepositional grain ages and multi-grain populations that are derived from the same source terrane. Although this method and its accuracy remains tenuous, when results from the K–S test are coupled with other results within this study, there is strong argument for the appropriateness of the K–S test on this particular dataset. If all samples and grain ages are compared, based on a CDF >0.05 (p-values using error in CDF with 95% confidence), then little similarity is noted between all samples, and only a handful of samples display any relatability. We recognise that a higher degree of similarity reflects stratigraphic proximity between samples, and we thus compared them accordingly, rather than the whole of the formation displaying source similarity.

Firstly, we assessed those samples that only represented stratigraphic position within the Cedar Mountain Formation: 1) uppermost Buckhorn Conglomerate; 2) uppermost Ruby Ranch; 3) middle Mussentuchit; 4) lowermost Naturita (Fig. 5a). Across all grain ages recovered from these four samples, the null hypothesis of similarity was rejected with all p-values at <0.00. If grains ages were restricted to <251.9 Ma (Mesozoic Grains only), samples from the middle Mussentuchit and the overlying lowermost Naturita displayed a p-value of 0.402, and the null hypothesis of similarity was accepted. We interpret the lack of similarity between members to reflect that: 1) although a major pre-Mesozoic detrital source is likely linked to the adjacent (Canyon Range, Pavant, Paxton phases) Sevier Thrust belt, there are other possible source terranes (for example Peace River); 2) there is support for the already suggested unconformities that are pervasive throughout the Cedar Mountain Formation; 3) the uppermost Mussentuchit is not present within the study area, rather it has been downcut by the Naturita; 4) sedimentation into this depo-centre pulsated, with an increasing frequency upsection.

A secondary assessment was carried out to test this pattern in the suite of fossil assemblages sites sampled throughout the Mussentuchit; and we find the pattern is confirmed (Fig 5b). The lowermost fossil site, Fortunate Son, has more genetic similarity with the uppermost Ruby Ranch (p-value of 0.582 for Mesozoic Grains) and is distinctly dissimilar to any of the fossil assemblage site overlying it (p-value of 0.00). By contrast, fossil assemblage sites in the middle and upper Mussentuchit indicate extremely high genetic similarity (Lindsay's Site with Deep Eddy (p-value 0.998)) or Mini Troll and Suicide Hill (p-value of 0.994) of Cretaceous grain ages. Even though all samples in the middle to upper Mussentuchit have high similarity, the p-value ranges from 0.106 to 0.994, and these differences in confidence correlate to differences in stratigraphic position. Furthermore, the subtle differences in p-value could also be reflecting temporally dissimilar volcanic inliers altogether ((southwest (Mogollon Highlands), the west (Sierra Nevada Batholith), and the northwest (Idaho Batholith)), rather than a singular, long-lived source.

4.4. Coeval and non-coeval volcanic-rich sedimentation

The above identification of episodic volcaniclastic and volcanilithic detrital input into the Mussentuchit is crucial, but requires a further detrital history detailing the synchronicity of detrital input directly or indirectly into the Last Chance depo-centre via various inliers of the westerly lying arc. In other localities across Utah, the Mussentuchit does preserve exceptional interbedded to lenticular

Table 3
Kolmogorov-Smirnov Test (K–S Test) Results, Note: Table displays “P” values with confirmed similarity of sources highlighted in gray (P > 5%) and negative results in white (P < 5%).

K-S P-values using error in the CDF

	Fortunate Son	Stormy Theropod	middle Mussentuchit	SLF	Deep Eddy	Suicide Hill	Mini Troll	Lindsay's Site	lowermost Naturita
Fortunate Son		0.000	0.000	0.000	0.000	0.000	0.000	0.000	0.000
Stormy Theropod	0.000		**0.082**	0.000	0.028	**0.502**	**0.516**	0.031	0.016
middle Mussentuchit	0.000	**0.082**		**1.000**	**0.932**	**0.584**	**0.441**	**0.998**	**0.930**
SLF	0.000	0.000	**1.000**		**0.457**	0.027	0.004	**0.878**	**0.183**
Deep Eddy	0.000	0.028	**0.932**	**0.457**		**0.172**	**0.106**	**0.998**	**0.754**
Suicide Hill	0.000	**0.502**	**0.584**	0.027	**0.172**		**0.994**	**0.404**	**0.590**
Mini Troll	0.000	**0.516**	**0.441**	0.004	**0.106**	**0.994**		**0.247**	**0.265**
Lindsay's Site	0.000	0.031	**0.998**	**0.878**	**0.998**	**0.404**	**0.247**		**0.801**
lowermost Naturita	0.000	0.016	**0.930**	**0.183**	**0.754**	**0.590**	**0.265**	**0.801**	

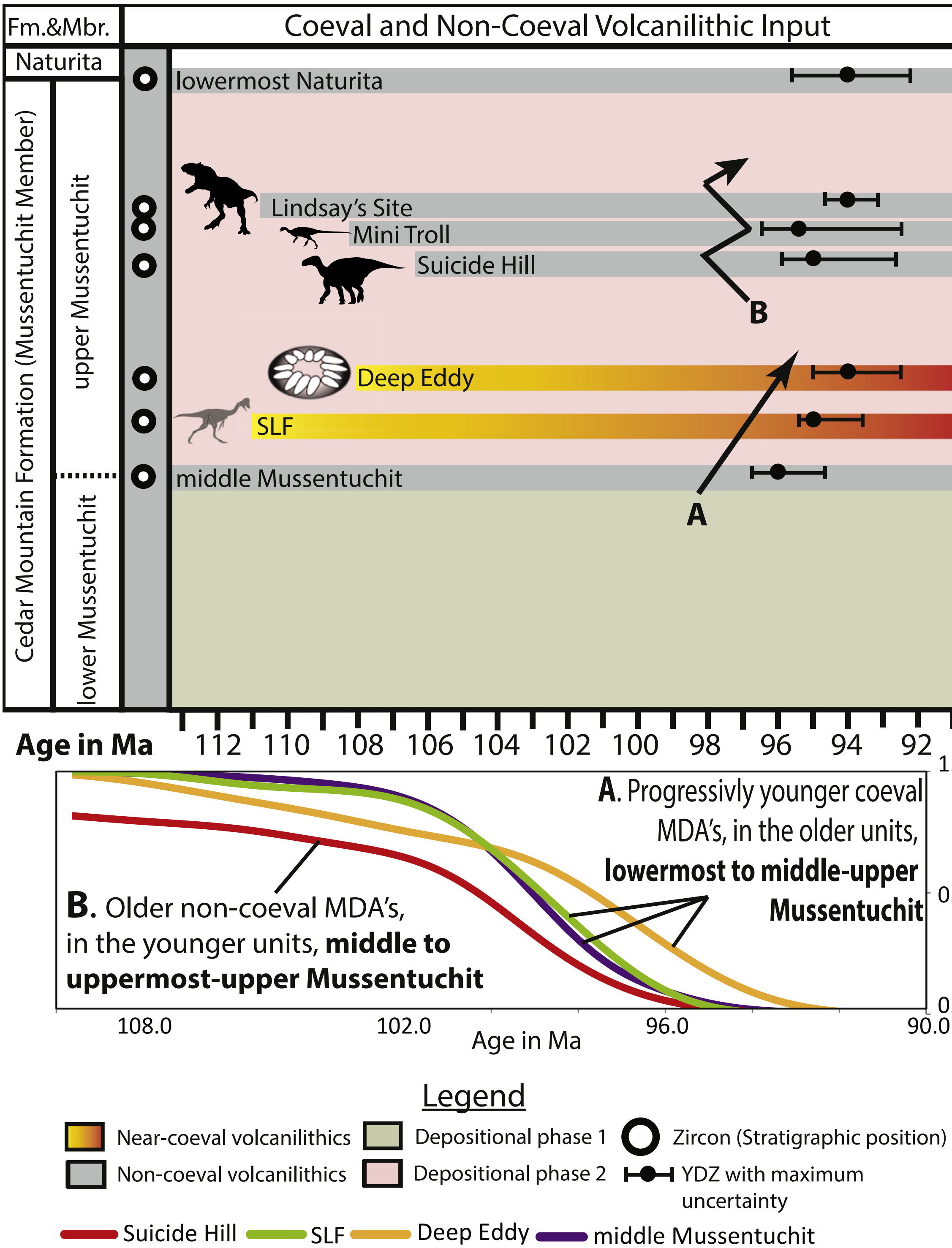

Fig. 8. Assessment of contemporaneity between coeval and non-coeval sedimentation within the Mussentuchit Member, along with the informal subdivision into a lower and upper sub-member. Corresponding K–S Test result displaying the coeval younger volcanilithic input in medial to very lowermost upper Mussentuchit overlain by older recycled volcanilithics. Adapted from Rossignol et al. (2019).

pyroclastic deposits in the form of smectitic ash horizon (Cifelli et al., 1997), identified as primary, syndepositional fine volcaniclastic material (in agreement with Kirkland et al., 2016 and references therein). However, the well-documented bentonitic nature of the Mussentuchit could provide volcanilithic histories to complement the volcaniclastic input histories from other localities in the member. As mentioned above, the recent publication by Rossignol et al. (2019) elegantly constrains sedimentation age via volcaniclastic rocks, yet this study seeks to apply a modified form of their method to volcanilithic-rich sediment. It should be noted, these are treated as detrital populations and require statistical support for interpreting MDAs and it's error, ergo utilizing YDZ. When both YSG and YDZ are plotted, the results mirror and support the observations by Coutts et al. (2019).

This study readily identifies several input patterns into the depo-centre by using the modified “Rossignol method” (Fig. 8). Firstly, this study identifies that each member is younging as it progresses upsection; however, we also readily several extensive unconformities, in agreement with Kirkland et al. (2016; and references therein). As with many sedimentation narratives, this is not a single-source history, nor a perfect trend, especially in the Mussentuchit Member. Although limited in resolution, the temporal gap between the uppermost Ruby Ranch Member (MDA at 109.9 ma; sample: uppermost Ruby Ranch) and the lowermost Mussentuchit Member sample (102.1 Ma; sample: Fortunate Son) indicate a disconformity of non-trivial duration (Kirkland et al., 2016; and references therein).

In reviewing the overall trend from the lowermost to uppermost portions of the Mussentuchit, the patterns roughly fit a model of contemporaneous volcanic activity and sedimentation. However, it is readily apparent upon closer inspection that there are different phases of non-coeval and coeval volcanic activity and sedimentation therein. This study identifies the input of volcanic detritus as non-coeval until the stratigraphic level of Stormy Theropod. Stormy Theropod is the oldest of our samples with grain ages from this lower stratigraphic section that are younger than 100 Ma, with the MDA ±96 Ma. Therefore, this single sample is likely not representative of a true coeval emplacement, but rather, a near-coeval emplacement within this particular depo-centre, and is stratigraphically close to syndepositional volcaniclastic $^{40}Ar/^{39}Ar$ dates of 98 Ma and 97-96 Ma in other areas of the exposed Mussentuchit (Cifelli et al., 1997, 1999; Garrison et al., 2007). Recycling likely continues thereafter, up unto the middle Mussentuchit.

Our study identifies a series of samples displaying clear signals of contemporaneity between volcanic activity and sedimentation into the Mussentuchit Wash depo-centre (middle to lowermost-upper Mussentuchit, samples: middle Mussentuchit, SLF, Deep Eddy, and Suicide Hill) (Fig. 8). Samples recovered from overlying units including Suicide Hill, Mini Troll, Lindsay's Site, along with the overlying contact with the Naturita Sandstone display overlapping uncertainties. Yet it is not possible to infer contemporaneity, likely due to a reworking phase of volcanilithic-rich sediment input rather than volcaniclastic synchronous emplacement. This trend is confirmed with the above mentioned K–S test. The samples middle Mussentuchit, SLF, Deep Eddy, contain progressively younger and coeval MDAs in older sediments, whereas younger, overlying units, including Suicide Hill, Mini Troll, Lindsay's Site contain older non-coeval MDAs in younger sediments (Fig. 8).

4.5. CA-TIMS and LA-ICP-MS data support

This study robustly identified multi-grain populations of post-Cenomanian ages that were incongruent with respect to the published temporal framework of the Mussentuchit Member, and the Cedar Mountain Formation as a whole (Kirkland et al., 2016; and references therein). Therefore, as a secondary check, this study utilized the CA-TIMS on both pre- and post-Cenomanian grains identified by the initial laser ablation (Table 1; Fig. 9). It was suspected that Pb loss occurred in 20+ grains falling within the Turonian (93.9 Ma or younger on the 206/238 U–Pb series) from multiple Mussentuchit samples, and this result required secondary investigation. Thus, three grains were selected from the lowermost Naturita sample ((Grains: 15 (94 ± 1.3 Ma), 45 (94 ± 1.4 Ma), and 50 (92 ± 1.3 Ma)) and four grains from Deep Eddy sample (Grains: 1 (94 ± 1.2 Ma), 11 (94 ± 1.5 Ma), 103 (92 ± 1.4), and 125 (89 ± 1.3 Ma)) (Table 1, Fig. 9) for secondary analysis. In the first round we analysed the lowermost Naturita grains 15, 45, and 50 which yielded dates of 96.12 ± 0.10, 95.64 ± 0.11, and 104.67 ± 0.13 Ma, respectively. The youngest grain is considered the maximum depositional age, in this case, MDA = 95.64 ± 0.11. To corroborate these initial results, four further grains, selected from the Deep Eddy sample were analysed. Grains 1, 11, 103, and 125 yielded dates of 99.68 ± 0.14, 100.59 ± 0.09, 99.82 ± 0.22 Ma, and 100.72 ± 0.12 Ma, respectively. The two youngest dates yielded a weighted mean of 99.72 ± 0.12/0.12/0.16 Ma (MSWD = 1.1, probability of fit = 0.30). This is considered the maximum depositional age. Thus, preliminary data suggest that grains with Turonian age (or younger) likely suffer from Pb loss and are in fact older than originally indicated. Therefore, this study finds reliable evidence that strongly indicates the Mussentuchit Member was emplaced during the terminal phase of the Cenomanian (Fig. 9).

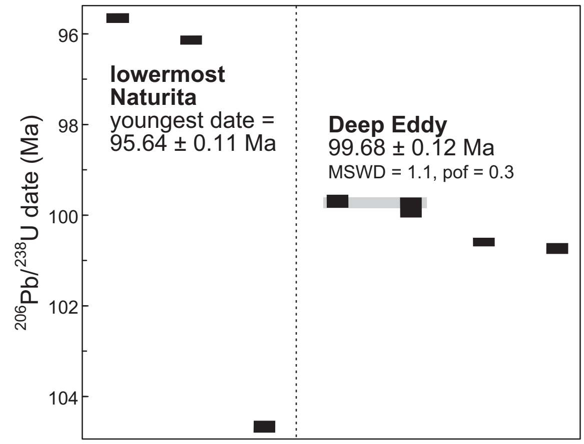

Fig. 9. Plot of $^{206}Pb/^{238}U$ dates from single grains of zircon analysed by CA-TIMS. Plotted with Isoplot 3.0 and 4.0 (Ludwig, 2003, 2009). Error bars are at 2 sigma. A weighted mean date is shown and represented by the grey box behind the error bars. Three zircon grains were analysed from the basal portion of the overlying Naturita Sandstone, likely composed of re-eroded and reworked upper Mussentuchit were analysed with 95.64 Ma found to be the youngest grain and is considered the CA-TIMS-based MDA; Four zircon grains from the Deep Eddy fossil locality were analysed, with the non-MDA to be around 99.68.

5. Discussion

This study sought to 1) refine the depositional age and the duration of sedimentation of the Mussentuchit Member within the Mussentuchit Wash depo-centre; 2) determine if the recovered volcanilithics are suitable to generate a robust temporal framework, while simultaneously determining if they represent non-coeval or coeval inputs; and, thus, can provide reliable MDAs; and 3) determine if it is reasonable to predict that the Mussentuchit contains a single temporally constrained assemblage or may, in fact, represent multiple, temporally distinguishable assemblages.

Our results identify that emplacement of volcanilithic-rich sediment within the Mussentuchit Member, in the areas of Mussentuchit Wash, occurred largely within the upper Cenomanian. Initial LA-ICP-MS analysis obtained seemingly concordant grain ages of Turonian age or younger; yet, the repeated occurrence of the youngest grain ages was sedimentologically and biostratigraphically incongruent. In a recent study by Herriott et al. (2019), the authors noted a distinct trend of Pb loss among the very youngest grains from each population and should be disregarded in subsequent calculations of MDAs. Therefore, to validate our MDA estimates and assess if these pre-Turonian grains suffer Pb loss, we secondarily measured multiple grains via CA-TIMS. In utilising the CA-TIMS, we confirmed that grain ages of 93.9 Ma or younger suffered from significant Pb loss, displaying vastly different ages than those reported via LA-ICP-MS, and therefore were rejected from this study. On the other hand, utilising the CA-TIMS confirmed our results for grain ages older 93.9 Ma via LA-ICP-

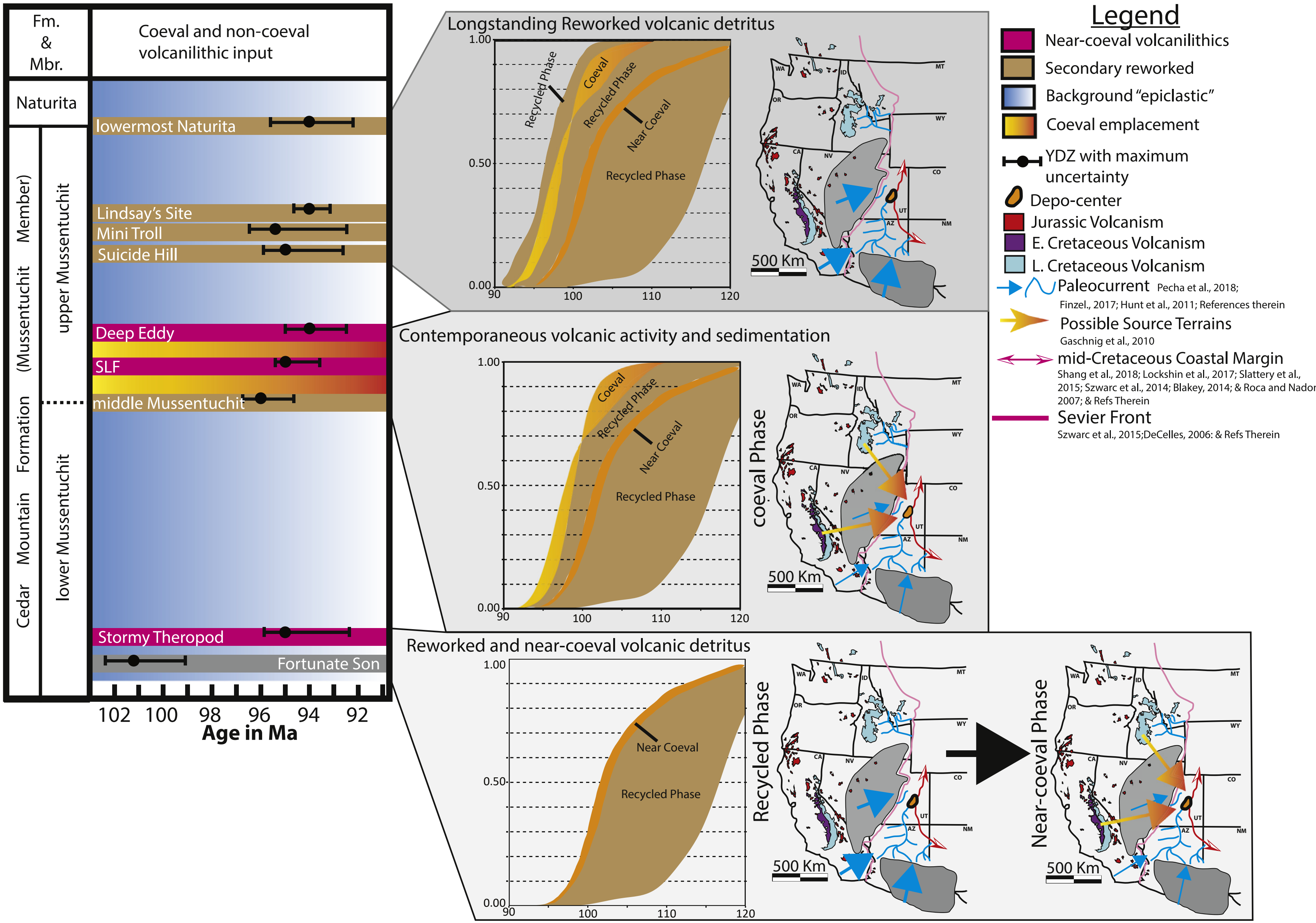

Fig. 10. Combination of coeval and non-coeval sediment input within the Mussentuchit Wash depo-centre and likely sources of active volcanic inliers during Phase A-C, within the westerly lying Cordilleran Arc.

MS, with grains ages very similar between to the two analytical methods (for example lower Mussentuchit zircon grain 45; LA-ICP-MS aged dated at 94 ± 1.4 and via CA-TIMS at 95.64 ± 0.11), and suffered only minimal to no Pb loss.

With this in mind, this study identifies only one reliable MDA in the lower Mussentuchit, near to 96 Ma. This would indicate a non-coeval relationship between volcanism and sedimentation (recycled and non-coeval) for much of the lower Mussentuchit. This is indirectly corroborated by Garrison et al. (2007 pg 476/Table 3), who identified a distinct overlapping age-ranges (lower ash - 98.2 Ma, middle ash - 96.7 Ma, and upper ash - 97.2 Ma). Based on Rossignol et al. (2019), these data would indicate a reworking or non-contemporaneous pattern of volcanilithic-rich sediment emplacement at the Cifelli #2 fossil quarry, rather than primary emplacement of volcaniclastic ash. Addressing this concern is beyond the scope of this particular study; but in 2019, our team resampled the volcaniclastic/volcanilithic horizons described by Cifelli et al. (1997,1999), including V695 and V826, and these are currently being re-assessed.

Contrary to underlying units, this study discovered that volcanilithic-rich sediment in the lowermost to middle upper Mussentuchit units yielded several reliable MDAs between 96 and 94 Ma. This series of MDAs from middle Mussentuchit, SLF, and Deep Eddy indicate contemporaneity between volcanism and sedimentation does occur up to the middle upper Mussentuchit. However, the uppermost Mussentuchit and the lowermost Naturita lack any reliable MDA's, rather samples indicate non-contemporaneity and reworking (Suicide Hill, Mini Troll, Lindsay's Site, and lowermost Naturita). This study recognises that the detrital grain-ages recovered from the lowermost portion of the Naturita Sandstone reflect secondary or even tertiary reworking, and this sedimentary event is likely younger than 94 Ma.

Our confirmed results were coupled with the K–S test, which further supported the paradigm that some samples were either non-coeval or coeval with sedimentation and confirmed the above mentioned MDAs. Combined with the K–S test, a pattern emerges in which samples displaying contemporaneity also having a higher likelihood of similar sources or volcanic events, yet samples that were identified as non-contemporaneous, displayed less genetic likelihood of being from the same source or volcanic event (Table 3). Furthermore, this study also identifies a distinct difference between pre-96 Ma populations and all others, with samples derived from the basal portions of the Mussentuchit Member (Fortunate Son) having no genetic similarity to any other samples tested. Secondly, this study notes that samples derived from the lower Mussentuchit (for example, Stormy Theropod) only displays weak genetic similarity to those from overlying strata. The only similarity of samples separated by stratigraphic differences is that of the Stormy Theropod and the Suicide Hill and Mini Troll localities (p-values at 0.502 and 0.516 respectively; Table 3). This is interpreted to indicate that the first emplacement of coeval grains with a grain age of 96 Ma occurs within Stormy Theropod, and the similarly aged grains in both Suicide Hill and Mini Troll are detrital. Interestingly, Stormy Theropod and it's MDA at 96 Ma as compared to that of the MDAs of 95 and 94 Ma from SLF and Deep Eddy, displays zero genetic similarity, indicating differential sources.

With all the above in mind, our study confidently confirms the above mentioned MDAs (Fig.10), which also indicate sedimentation of the Mussentuchit Member, minimally occurred in two distinct phases, over a 2 Myr span. This indicates at least two distinct possible scenarios: 1) if these zircons are derived from the same volcanic inlier within the westerly lying arc (for example the Sierra Nevada Batholith), then this would indicate two phases of volcanism, which lacked the intensity to emplace primary volcaniclastics, and are recorded only as eroded volcanilithics; or 2) the MDAs of 96 and 94 Ma indicate different volcanic inliers altogether (Sierra Crest, Owhyee, Idaho Batholith, among others); yet both within the westerly lying Cordilleran Arc, in agreement with DeCelles and Graham (2015) (Fig. 10). Furthermore, this study can conclude that reworked non-coeval volcanilithics would likely be from volcanic Phases A (160–140 Myr) and B (140–105 Myr), whereas, near-coeval and coeval volcanics would be from the early- and mid-C Phase (105–80 Myr) (DeCelles and Graham, 2015). Lastly, this study can indicate that these stratigraphically different MDAs not only represent different source terranes (different inliers within the westerly lying arc), but more confidently interpret the two depositional phases. A synthesis of the above data, along with sedimentological evidence argues for informally subdividing the Mussentuchit into lower and upper sub-members.

While we recognise that this needs to be extensively and rigorously tested, these data provide a stratigraphic framework for testing the hypothesis that faunal assemblages within the lower Mussentuchit are distinct from those in the upper Mussentuchit. The reader must bear in mind that these results, however robust, are localised to the Mussentuchit Wash. In consideration of regional context, it is more than likely that sediment emplacement across the Mussentuchit Member and the whole of the Cedar Mountain Formation is temporally variable. Yet, in a regional tectonic framework, the termination “or erosion” of the uppermost Mussentuchit sedimentary package prior to the regional kinematic jump of the westerly lying Sevier Thrust Belt in the Turonian seems reasonable (DeCelles and Graham, 2015: fig2).

6. Conclusions

We present a revised, localized chronostratigraphic framework for the exposed Mussentuchit Member of the Cedar Mountain Formation, in the region surrounding Mussentuchit Wash, central Utah. The combination of both LA-ICP-MS and CA-TIMS data, along with seven numerical methods and additional provenance tools, provides a confident assessment of the MDAs for the upper and lower sediments of the Mussentuchit Member in this area. We find that the sediments surrounding Mussentuchit Wash were deposited no earlier than the upper Cenomanian, spanning an age interval of 96–94 Myr. Furthermore, by coupling well-established non-paremetric Kolmogorov-Smirnov tests with novel methods for assessing contemporaneity between sedimentation and volcanism, we identify at least two pulses of sediment input into Mussentuchit Wash depo-centre. The first coeval volcanic input occurs in basal portions of the lower Mussentuchit Member, followed by a non-coeval recycling phases. The second coeval volcanic input occurs in very basal portions of the upper Mussentuchit and a repeated non-coeval volcanism and epiclastics. This two-phase depositional cycle preserved in the uppermost Cedar Mountain Formation occurred no later than the terminal phase of the Cenomanian, likely linked to the onset of the next phase of thrusting to the west. It is likely that the later-phased sedimentation in the Mussentuchit can be linked to embryonic development of the Last Chance Delta, but occurs before Turonian thrusting of the westerly lying Sevier Belt (Bhattacharya and MacEachern, 2009). Finally, our data indicate that two temporally disjunct fossil assemblages are preserved within the lower and upper Mussentuchit Member, respectively, prompting hypotheses of faunal dissimilarity across the member. Testing this hypothesis will require refined stratigraphic occurrence data for all vertebrate localities within the Mussentuchit recovered to date, as well as detailed anatomical investigations of taxa known from multiple skeletal remains spanning upper and lower sediments. Our future investigations will seek to broaden and re-examine the findings of this study in a regional context, along with testing broad-scale correlations including those recently published for the Cloverly Formation to the northeast in Wyoming (D'Emic et al., 2019).

Acknowledgements

We thank staff, students, and volunteers of the 2015–2019 expeditions for repeated explorations of the Mussentuchit Member; M. Leschin, S. Foss, G. McDonald, R. Hunt-Foster, J. Kirkland, M. Hayden, J. Krishna, R. Irmis, staff of the Price Field Office, the Bureau of Land Management Utah State Office, Natural History Museum of Utah, and Utah Geological Survey for permitting and expedition support. Special thanks go to R. Rossouw, and L. Bracciali of the Central Analytical Facility at Stellenbosch University and Huang, H., at the Advanced Analytical Centre at James Cook University during preparation and data reduction of LA-ICP-MS data, along with J. Crowley at the Department of Geological Sciences at Boise State University for CA-TIMS analysis and data reduction. Financial support was provided by Stellenbosch University's Department of Earth Sciences (RSA), SU-DRD Fund (RSA), F. Kruger (MyBrew) (RSA), North Carolina Museum of Natural Sciences (USA), the Canyonlands Natural History Association (USA). Lastly we would like to especially thank the editor and both anonymous reviewers, whose comments and alterations greatly strengthened this manuscript to its current state.

References

Amidon, W.H., Burbank, D.W., Gehrels, G.E., 2005a. U–Pb zircon ages as a sediment mixing tracer in the Nepal Himalaya. Earth and Planetary Science Letters 235 (1–2), 244–260.

Amidon, W.H., Burbank, D.W., Gehrels, G.E., 2005b. Construction of detrital mineral populations: Insights from mixing of U-Pb zircon ages in Himalayan rivers. Basin Research 17 (4), 463–485.

Arens, N.C., Harris, E.B., 2015. Paleoclimatic reconstruction for the Albian–Cenomanian transition based on a dominantly angiosperm flora from the Cedar Mountain Formation, Utah, USA. Cretaceous Research 53, 140–152.

Avrahami, H.M., Makovicky, P.J., Zanno, L.E., 2019. Paleohistology Of A New Orodromine From The Upper Cretaceous (Cenomanian) Mussentuchit Member Of The Cedar Mountain Formation, Utah; Histological Implications For Burrowing Behavior. Journal of Vertebrate Paleontology Programs Abstracts 2019, 56.

Barbeau Jr., D.L., Gombosi, D.J., Zahid, K.M., Bizimis, M., Swanson-Hysell, N., Valencia, V., Gehrels, G.E., 2009. U-Pb zircon constraints on the age and provenance of the Rocas Verdes basin fill, Tierra del Fuego, Argentina. Geochemistry, Geophysics, Geosystems 10 (12).

Bhattacharya, J.P., MacEachern, J.A., 2009. Hyperpycnal rivers and prodeltaic shelves in the Cretaceous seaway of North America. Journal of Sedimentary Research 79 (4), 184–209.

Blakey, R.C., 2014. Paleogeography and paleotectonics of the Western Interior Seaway, Jurassic-Cretaceous of North America. Search and Discovery 30392, 72.

Britt, B.B., Burton, D., Greenhalgh, B.W., Kowallis, B., Christiansen, E., Chure, D.J., 2007. Detrital zircon ages for the basal Cedar Mountain Formation (Early Cretaceous) near Moab, and Dinosaur National Monument, Utah. In Geological Society of America Abstracts with Programs 39 (5), 16.

Britt, B.B., Eberth, D.A., Scheetz, R.D., Greenhalgh, B.W., Stadtman, K.L., 2009. Taphonomy of debris-flow hosted dinosaur bonebeds at Dalton Wells, Utah (Lower Cretaceous, Cedar Mountain Formation, USA). Palaeogeography, Palaeoclimatology, Palaeoecology 280 (1–2), 1–22.

Brown, K.L., Hart, W.K., Stuck, R.J., 2018. Temporal and geochemical signatures in granitoids of northwestern Nevada: Evidence for the continuity of the Mesozoic magmatic arc through the western Great Basin. Lithosphere 10 (2), 327–350.

Burton, D., Greenhalgh, B.W., Britt, B.B., Kowallis, B.J., Elliot, W., 2006. New radiometric ages from the Cedar Mountain Formation, Utah and the Cloverly Formation, Wyoming: implications for contained dinosaur faunas. In Geological Society of America Abstracts with Programs 38 (7).

Cawood, P.A., Hawkesworth, C.J., Dhuime, B., 2012. Detrital zircon record and tectonic setting. Geology 40 (10), 875–878.

Chure, D., Britt, B.B., Whitlock, J.A., Wilson, J.A., 2010. First complete sauropod dinosaur skull from the Cretaceous of the Americas and the evolution of sauropod dentition. Naturwissenschaften 97 (4), 379–391.

Cifelli, R.L., Kirkland, J.I., Weil, A., Deino, A.L., Kowallis, B.J., 1997. High-precision 40Ar/39Ar geochronology and the advent of North America's Late Cretaceous terrestrial fauna. Proceedings of the National Academy of Sciences 94 (21), 11163–11167.

Cifelli, R.L., Nydam, R.L., Gardner, J.D., Weil, A., Eaton, J.G., Kirkland, J.I., Madsen, S.K., Gillette, D.D., 1999. Medial Cretaceous vertebrates from the Cedar Mountain Formation, Emery County, Utah: the Mussentuchit local fauna. Vertebrate paleontology in Utah 99 (1), 219–242.

Cohen, K.M., Finney, S.C., Gibbard, P.L., Fan, J.X., 2013. The ICS international chronostratigraphic chart. Episodes 36 (3), 199–204 v2019/05.

Condon, D.J., Schoene, B., McLean, N.M., Bowring, S.A., Parrish, R.R., 2015. Metrology and traceability of U–Pb isotope dilution geochronology (EARTHTIME Tracer Calibration Part I). Geochimica et Cosmochimica Acta 164, 464–480.

Corfu, F., Hanchar, J.M., Hoskin, P.W.O., Kinny, P., 2003. Atlas of zircon textures. Reviews in Mineralogy and Geochemistry 53, 469–500.

Coutts, D.S., Matthews, W.A., Hubbard, S.M., 2019. Assessment of widely used methods to derive depositional ages from detrital zircon populations. Geoscience Frontiers 10 (4), 1421–1435.

Crowley, J.L., Schoene, B., Bowring, S.A., 2007. U-Pb dating of zircon in the Bishop Tuff at the millennial scale. Geology 35, 1123–1126.

Currie, B.S., 1997. Sequence stratigraphy of nonmarine Jurassic–Cretaceous rocks, central Cordilleran foreland-basin system. The Geological Society of America Bulletin 109 (9), 1206–1222.

Currie, B.S., 2002. Structural configuration of the Early Cretaceous Cordilleran foreland-basin system and Sevier thrust belt, Utah and Colorado. The Journal of Geology 110 (6), 697–718.

DeCelles, P.G., 2004. Late Jurassic to Eocene evolution of the Cordilleran thrust belt and foreland basin system, western USA. American Journal of Science 304 (2), 105–168.

DeCelles, P.G., Burden, E.T., 1992. Non-marine sedimentation in the overfilled part of the Jurassic-Cretaceous Cordilleran foreland basin: Morrison and Cloverly Formations, central Wyoming, USA. Basin Research 4 (3–4), 291–313.

DeCelles, P.G., Lawton, T.F., Mitra, G., 1995. Thrust timing, growth of structural culminations, and synorogenic sedimentation in the type Sevier orogenic belt, western United States. Geology 23 (8), 699–702.

DeCelles, P.G., Currie, B.S., 1996. Long-term sediment accumulation in the Middle Jurassic–early Eocene Cordilleran retroarc foreland-basin system. Geology 24 (7), 591–594.

DeCelles, P.G., Coogan, J.C., 2006. Regional structure and kinematic history of the Sevier fold-and-thrust belt, central Utah. The Geological Society of America Bulletin 118 (7–8), 841–864.

DeCelles, P.G., Graham, S.A., 2015. Cyclical processes in the North American Cordilleran orogenic system. Geology 43 (6), 499–502.

DeGraaff-Surpless, K., Mahoney, J.B., Wooden, J.L., McWilliams, M.O., 2003. Lithofacies control in detrital zircon provenance studies: Insights from the Cretaceous Methow basin, southern Canadian Cordillera. The Geological Society of America Bulletin 115 (8), 899–915.

D'Emic, M.D., Foreman, B., Jud, N.A., Britt, B.B., Schmitz, M., Crowley, J.L., 2019. Chronostratigraphic revision of the cloverly formation (Lower Cretaceous, Western Interior, USA). Bulletin of the Peabody Museum of Natural History 60 (1), 3–40.

Dickinson, W.R., Gehrels, G.E., 2003. U–Pb ages of detrital zircons from Permian and Jurassic eolian sandstones of the Colorado Plateau, USA: paleogeographic implications. Sedimentary Geology 163 (1–2), 29–66.

Dickinson, W.R., Gehrels, G.E., 2008. Sediment delivery to the Cordilleran foreland basin: Insights from U-Pb ages of detrital zircons in Upper Jurassic and Cretaceous strata of the Colorado Plateau. American Journal of Science 308 (10), 1041–1082.

Dickinson, W.R., Gehrels, G.E., 2010. Insights into North American paleogeography and paleotectonics from U–Pb ages of detrital zircons in Mesozoic strata of the Colorado Plateau, USA. International Journal of Earth Sciences 99 (6), 1247–1265.

Dickinson, W.R., Gehrels, G.E., 2009a. U-Pb ages of detrital zircons in Jurassic eolian and associated sandstones of the Colorado Plateau: Evidence for transcontinental dispersal and intraregional recycling of sediment. The Geological Society of America Bulletin 121 (3–4), 408–433.

Dickinson, W.R., Gehrels, G.E., 2009b. Use of U–Pb ages of detrital zircons to infer maximum depositional ages of strata: a test against a Colorado Plateau Mesozoic database. Earth and Planetary Science Letters 288 (1–2), 115–125.

Dilcher, D., 2000. Toward a new synthesis: major evolutionary trends in the angiosperm fossil record. Proceedings of the National Academy of Sciences 97 (13), 7030–7036.

Driebergen, J., Cifelli, R., Zanno, L.E., Makovicky, P.J., 2017. Comparitive Taphonomy of two juvenile *Eolambia caroljonesa* (Hadrosauria) Bonebeds from the Cedar Mountain Formation of Utah. Journal of Vertebrate Paleontology Programs Abstracts 2017, 105.

Eberth, D.A., Britt, B.B., Scheetz, R., Stadtman, K.L., Brinkman, D.B., 2006. Dalton Wells: Geology and significance of debris-flow-hosted dinosaur bonebeds in the Cedar Mountain Formation (Lower Cretaceous) of eastern Utah, USA. Palaeogeography, Palaeoclimatology, Palaeoecology 236 (3–4), 217–245.

Eberth, D.A., Miall, A.D., 1991. Stratigraphy, sedimentology and evolution of a vertebrate-bearing, braided to anastomosed fluvial system, Cutler Formation (Permian-Pennsylvanian), north-central New Mexico. Sedimentary Geology 72 (3–4), 225–252.

Elderbak, K., Leckie, R.M., Tibert, N.E., 2014. Paleoenvironmental and paleoceanographic changes across the Cenomanian–Turonian Boundary Event (Oceanic Anoxic Event 2) as indicated by foraminiferal assemblages from the eastern margin of the Cretaceous Western Interior Sea. Palaeogeography, Palaeoclimatology, Palaeoecology 413, 29–48.

Eldrett, J.S., Ma, C., Bergman, S.C., Lutz, B., Gregory, F.J., Dodsworth, P., Phipps, M., Ramezani, J., 2015. An astronomically calibrated stratigraphy of the

Cenomanian, Turonian and earliest Coniacian from the Cretaceous Western Interior Seaway, USA: Implications for global chronostratigraphy. Cretaceous Research 56, 316–344.
Fastovsky, D.E., Huang, Y., Hsu, J., Martin-McNaughton, J., Sheehan, P.M., Weishampel, D.B., 2004. Shape of Mesozoic dinosaur richness. Geology 32 (10), 877–880.
Fedo, C.M., Sircombe, K.N., Rainbird, R.H., 2003. Detrital zircon analysis of the sedimentary record. Reviews in Mineralogy and Geochemistry 53 (1), 277–303.
Finzel, E.S., 2017. Detrital Zircon microtectures and U-PB geochronology of Upper Jurassic to Paleocene strata in the distal North American Cordillera forland basin. Tectonics 36, 1295–1316.
Gaschnig, R.M., Vervoort, J.D., Lewis, R.S., McClelland, W.C., 2009. Migrating magmatism in the US cordillera: in situ U-Pb geochronology of the Idaho Batholith. Contributions to Mineralogy and Petrology 159, 863–883.
Gaschnig, R.M., Vervoort, J.D., Lewis, R.S., McClelland, W.C., 2010. Migrating magmatism in the northern US Cordillera: in situ U–Pb geochronology of the Idaho batholith. Contributions to Mineralogy and Petrology 159 (6), 863–883.
Gaschnig, R.M., Vervoort, J.D., Tikoff, B., Lewis, R.S., 2017. Construction and preservation of batholiths in the northern US Cordillera. Lithosphere 9 (2), 315–324.
Gehrels, G.E., Dickinson, W.R., Ross, G.M., Stewart, J.H., Howell, D.G., 1995. Detrital zircon reference for Cambrian to Triassic miogeoclinal strata of western North America. Geology 23 (9), 831–834.
Gehrels, G., Pecha, M., 2014. Detrital zircon U-Pb geochronology and Hf isotope geochemistry of Paleozoic and Triassic passive margin strata of western North America. Geosphere 10 (1), 49–65.
Gehrels, G., Rusmore, M., Woodsworth, G., Crawford, M., Andronicos, C., Hollister, L., Patchett, J., Davidson, C., 2009. U-Th-Pb geochronology of the Coast Mountains batholith in north-coastal British Columbia: Constraints on age and tectonic evolution. The Geological Society of America Bulletin 121 (9–10), 1341–1361.
Gehrels, G., 2011. Detrital zircon U-Pb geochronology: Current methods and new opportunities. Tectonics of Sedimentary Basins: Recent Advances 45–62.
Garrison Jr., J.R., Brinkman, D., Nichols, D.J., Layer, P., Burge, D., Thayn, D., 2007. A multidisciplinary study of the Lower Cretaceous Cedar Mountain Formation, Mussentuchit Wash, Utah: a determination of the paleoenvironment and paleoecology of the Eolambia caroljonesa dinosaur quarry. Cretaceous Research 28 (3), 461–494.
Gerstenberger, H., Haase, G., 1997. A highly effective emitter substance for mass spectrometric Pb isotope ratio determinations. Chemical Geology 136, 309–312.
Gradstein, F.M., Agterberg, F.P., Ogg, J.G., Hardenbol, J., Van Veen, P., Thierry, J., Huang, Z., 1995. A Triassic, Jurassic and Cretaceous time scale. In: Berggren, W.A., Kent, D.v., Aubry, M.P., Hardenbol, J. (Eds.), Geochronology, time scales and global stratigraphic correlation: SEPM Special Publiction, vol. 54, pp. 95–126.
Greenhalgh, B.W., Britt, B.B., 2007. Stratigraphy and sedimentology of the Morrison–Cedar Mountain Formation boundary, east-central Utah.
Guynn, J., Gehrels, G., 2010. Comparison of detrital zircon age distributions using the KS test. University of Arizona, Tucson.
Hay, W.W., Floegel, S., 2012. New thoughts about the Cretaceous climate and oceans. Earth-Science Reviews 115 (4), 262–272.
Hedges, S.B., Parker, P.H., Sibley, C.G., Kumar, S., 1996. Continental breakup and the ordinal diversification of birds and mammals. Nature 381 (6579), 226.
Hendrix, B., Moeller, A., Ludvigson, G.A., Joeckel, R.M., Kirkland, J.I., 2015. A new approach to date paleosols in terrestrial strata: a case study using U-Pb zircon ages for the Yellow Cat Member of the Cedar Mountain Formation of eastern Utah. In Geological Society of America, Abstracts with Programs 47 (7).
Herriott, T.M., Crowley, J.L., Schmitz, M.D., Wartes, M.A., Gillis, R.J., 2019. accepted, Exploring the law of detrital zircon: LA-ICP-MS and CA-TIMS geochronology of Jurassic forearc strata, Cook Inlet. Geology, Alaska, USA 47 (11), 1044–1048.
Herzog, L.L., Zanno, L.E., Makovicky, P.J., 2015. New Solemydid turtle specimens from the Upper Cretaceous Mussentuchit Member of the Cedar Mountain Formation. Journal of Vertebrate Paleontology Programs Abstracts 2015, 142.
Hietpas, J., Samson, S., Moecher, D., Chakraborty, S., 2011. Enhancing tectonic and provenance information from detrital zircon studies: assessing terrane-scale sampling and grain-scale characterization. Journal of the Geological Society 168 (2), 309–318.
Hoffman, P.F., 1988. United plates of America, the birth of a craton: Early Proterozoic assembly and growth of Laurentia. Annual Review of Earth and Planetary Sciences 16 (1), 543–603.
Horstwood, M.S.A., Košler, J., Gehrels, G., Jackson, S.E., McLean, N.M., Paton, C., Pearson, N.J., Sircombe, K., Sylvester, P., Vermeesch, P., Bowring, J.F., Condon, D.J., Schoene, B., 2016. Community-Derived Standards for LA-ICP-MS U-(Th-)Pb Geochronology – Uncertainty Propagation, Age Interpretation and Data Reporting. Geostandards and Geoanalytical Research 40 (3), 301–332.
Hunt, G.J., Lawton, T.F., Kirkland, J.I., Sprinkel, D.A., Yonkee, W.A., Chidsey, T.C., 2011. Detrital zircon U-Pb geochronological provenance of Lower Cretaceous strata, foreland basin, Utah. Sevier Thrust Belt: Northern and Central Utah and Adjacent Areas: Utah Geological Association, Publication 40, 193–211.
Jackson, S.E., Pearson, N.J., Griffin, W.L., Belousova, E.A., 2004. The application of laser ablation-inductively coupled plasma-mass spectrometry to in situ U–Pb zircon geochronology. Chemical Geology 211 (1–2), 47–69.
Jaffey, A.H., Flynn, K.F., Glendenin, L.E., Bentley, W.C., Essling, A.M., 1971. Precision measurements of half-lives and specific activities of ^{235}U and ^{238}U. Physical Review C 4, 1889–1906.
Jinnah, Z.A., Roberts, E.M., Deino, A.L., Larsen, J.S., Link, P.K., Fanning, C.M., 2009. New 40Ar-39Ar and detrital zircon U-Pb ages for the Upper Cretaceous Wahweap and Kaiparowits formations on the Kaiparowits Plateau, Utah: implications for regional correlation, provenance, and biostratigraphy. Cretaceous Research 30 (2), 287–299.
Joeckel, R.M., Ludvigson, G.A., Möller, A., Hotton, C.L., Suarez, M.B., Suarez, C.A., Sames, B., Kirkland, J.I., Hendrix, B., 2019. Chronostratigraphy and terrestrial palaeoclimatology of Berriasian–Hauterivian strata of the Cedar Mountain Formation, Utah, USA. Geological Society, London, Special Publications 498, SP498–SP2018.
Johnson-Ransom, E., Makovicky, P.J., Zanno, L.E., Shimada, K., 2017. New coelurosaurian remains (Dinosauria: Theropoda) from the Cenomanian Mussentuchit Member of the Cedar Mountain Formation, Utah, USA. Journal of Vertebrate Paleontology Programs Abstracts 2017, 138.
Johnston, S., Gehrels, G., Valencia, V., Ruiz, J., 2009. Small-volume U–Pb zircon geochronology by laser ablation-multicollector-ICP-MS. Chemical Geology 259 (3–4), 218–229.
Kauffman, E.G., Caldwell, W.G.E., 1993. The Western Interior Basin in space and time. Evolution of the Western Interior Basin, vol. 39. Geological Association of Canada, Special Paper, pp. 1–30.
Katich Jr., P.J., 1951. Recent Evidence for Lower Cretaceous Deposits in Colorado Plateau. AAPG Bulletin 35 (9), 2093–2094.
Kirkland, J.I., 1992. Dinosaurs define a two-fold Lower Cretaceous zonation of the Cedar Mountain Formation, central Utah. In: Geological Society of America, Abstracts with Programs, vol. 24, p. 22.
Kirkland, J.I., Britt, B., Burge, D.L., Carpenter, K., Cifelli, R., DeCourten, F., Eaton, J., Hasiotis, S., Lawton, T., 1997. Lower to middle Cretaceous dinosaur faunas of the central Colorado Plateau: a key to understanding 35 million years of tectonics, sedimentology, evolution, and biogeography, vol. 42. Brigham Young University Geology Studies, pp. 69–104.
Kirkland, J.I., Cifelli, R.L., Britt, B.B., Burge, D.L., DeCourten, F.L., Eaton, J.G., Parrish, J.M., Gillette, D.D., 1999. Distribution of vertebrate faunas in the Cedar Mountain Formation, east-central Utah. Vertebrate paleontology in Utah 99 (1), 201.
Kirkland, J.I., Madsen, S.K., 2007. The Lower Cretaceous Cedar Mountain Formation eastern Utah.
Kirkland, J.I., Farlow, J.O., 2012. Dinosaurs and Geologic Time. The Complete Dinosaur 225.
Kirkland, J.I., Suarez, M., Suarez, C., Hunt-Foster, R., 2016. The Lower Cretaceous in East-Central Utah—The Cedar Mountain Formation and its Bounding Strata. Geology of the Intermountain West 3, 101–228.
Krogh, T.E., 1973. A low contamination method for hydrothermal decomposition of zircon and extraction of U and Pb for isotopic age determination. Geochimica et Cosmochimica Acta 37, 485–494.
Laskowski, A.K., DeCelles, P.G., Gehrels, G.E., 2013. Detrital zircon geochronology of Cordilleran retroarc foreland basin strata, western North America. Tectonics 32 (5), 1027–1048.
Lawrence, R.L., Cox, R., Mapes, R.W., Coleman, D.S., 2011. Hydrodynamic fractionation of zircon age populations. Bulletin 123 (1–2), 295–305.
Lawton, T.F., Hunt, G.J., Gehrels, G.E., 2010. Detrital zircon record of thrust belt unroofing in Lower Cretaceous synorogenic conglomerates, central Utah. Geology 38 (5), 463–466.
Lawton, T.F., Bradford, B.A., 2011. Correlation and provenance of Upper Cretaceous (Campanian) fluvial strata, Utah, USA, from zircon U-Pb geochronology and petrography. Journal of Sedimentary Research 81 (7), 495–512.
Leckie, R.M., Kirkland, J.I., Elder, W.P., 1997. Stratigraphic framework and correlation of a principal reference section of the Mancos Shale (Upper Cretaceous), Mesa Verde, Colorado. In: New Mexico Geological Society Guidebook, 48th Field Conference, Mesozoic Geology and Paleontology of the Four Corners Region, pp. 163–216.
Linde, G.M., Trexler Jr., J.H., Cashman, P.H., Gehrels, G., Dickinson, W.R., 2016. Detrital zircon U-Pb geochronology and Hf isotope geochemistry of the Roberts Mountains allochthon: New insights into the early Paleozoic tectonics of western North America. Geosphere 12 (3), 1016–1031.
Lloyd, G.T., Davis, K.E., Pisani, D., Tarver, J.E., Ruta, M., Sakamoto, M., Hone, D.W.E., Jennings, R., Benton, M.J., 2008. Dinosaurs and the Cretaceous terrestrial revolution. Proceedings of the Royal Society B: Biological Sciences 275 (1650), 2483–2490.
Lockshin, S.N., Yacobucci, M.M., Gorsevski, P., Gregory, A., 2017. Spatial characterization of cretaceous Western Interior Seaway paleoceanography using foraminifera, fuzzy sets and Dempster–Shafer theory. GeoResJ 14, 98–120.
Ludvigson, Greg A., Joeckel, R.M., Gonzalez, L.A., Gulbranson, E.L., Rasbury, E.T., Hunt, G.J., Kirkland, J.I., Madsen, S., 2010. Correlation of Aptian-Albian carbon isotope excursions in continental strata of the Cretaceous foreland basin, eastern Utah, USA. Journal of Sedimentary Research 80 (11), 955–974.
Ludvigson, G.A., Joeckel, R.M., Murphy, L.R., Stockli, D.F., Gonzalez, L.A., Suarez, C.A., Kirkland, J.I., Al-Suwaidi, A., 2015. The emerging terrestrial record of Aptian-Albian global change. Cretaceous Research 56, 1–24.
Lowery, C.M., Leckie, R.M., Bryant, R., Elderbak, K., Parker, A., Polyak, D.E., Schmidt, M., Snoeyenbos-West, O., Sterzinar, E., 2018. The Late Cretaceous Western Interior Seaway as a model for oxygenation change in epicontinental restricted basins. Earth-Science Reviews 177, 545–564.

Ludwig, K.R., 2003. User's Manual for Isoplot 3.00. Berkeley Geochronology Center, Berkeley, CA, p. 70.
Ludwig, K.R., 2009. Isoplot v. 4 for Excel 2007. Berkeley Geochronol. Cent., Berkeley, Calif.
Makovicky, P.J., Shinya, A., Zanno, L.E., 2014. New additions to the diversity of the Mussentuchit Member, Cedar Mountain Formation, Dinosaur Fauna. Journal of Vertebrate Paleontology Programs Abstracts 2014, 175.
Makovicky, P.J., Zanno, L.E., Gates, T.A., 2015. The Advent of North America's Late Cretaceous Fauna Revisited: Insights from New Discoveries and Improved Phylogenies. Journal of Vertebrate Paleontology Programs Abstracts 2015, 172–173.
Mattinson, J.M., 2005. Zircon U-Pb chemical abrasion ("CA-TIMS") method: combined annealing and multi-step partial dissolution analysis for improved precision and accuracy of zircon ages. Chemical Geology 220, 47–66.
May, S.R., Gray, G.G., Summa, L.L., Stewart, N.R., Gehrels, G.E., Pecha, M.E., 2013. Detrital zircon geochronology from the Bighorn Basin, Wyoming, USA: Implications for tectonostratigraphic evolution and paleogeography. Bulletin 125 (9–10), 1403–1422.
Miall, A.D., 1977. Lithofacies types and vertical profile models in braided river deposits: a summary.
Miall, A.D., 1985. Architectural-element analysis: a new method of facies analysis applied to fluvial deposits. Earth-Science Reviews 22 (4), 261–308.
Miall, A.D., 2014. In: Fluvial depositional systems, vol. 14. Springer, Berlin.
Miall, A.D., Catuneanu, O., 2019. The Western interior basin. In: The sedimentary basins of the United States and Canada. Elsevier, pp. 401–443.
Morath, P., Calvert, L., White, T., 2015. A chemostratigraphic model for the development of parasequences and its application to sequence stratigraphy and paleoceanography, Cretaceous Western Interior Basin, USA. In Chemostratigraphy 215–245.
Nasdala, L., Corfu, F., Valley, J.W., Spicuzza, M.J., Wu, F.Y., Li, Q.L., Yang, Y.H., Reiners, P.W., 2016. Zircon M127–A homogeneous reference material for SIMS U–Pb geochronology combined with hafnium, oxygen and, potentially, lithium isotope analysis. Geostandards and Geoanalytical Research 40 (4), 457–475.
Nesbitt, S.J., Denton, R.K., Loewen, M.A., Brusatte, S.L., Smith, N.D., Turner, A.H., Kirkland, J.I., McDonald, A.T., Wolfe, D.G., 2019. A mid-Cretaceous tyrannosauroid and the origin of North American end-Cretaceous dinosaur assemblages. Nature ecology & evolution 3 (6), 892.
Nichols, D.J., Sweet, A.R., 1993. Biostratigraphy of Upper Cretaceous non-marine plynofloras in a north-south transect of the Western Interior Basin. In: Caldwell, W.G.E., Kauffman, E.G. (Eds.), Evolution of the Western Interior Basin: Geological Association of Canada Special Paper, pp. 55–63.
Obradovich, J.D., 1993. A Cretaceous time scale. In: Caldwell, W.G.E., Kauffman, E.G. (Eds.), Evolution of the Western Interior Basin, vol. 39. Geological Association of Canada, Special Paper, pp. 379–396.
Paton, C., Hellstrom, J., Paul, B., Woodhead, J., Hergt, J., 2011. Iolite: freeware for the visualisation and processing of mass spectrometric data. Journal of Analytical Atomsphere Spectrometer. 26, 2508–2518.
Petrus, J.A., Kamber, B.S., 2012. VizualAge: A Novel Approach to Laser Ablation ICP-MS U-Pb Geochronology Data Reduction. Geostandards and Geoanalytical Research 36, 247–270.
Pecha, M.E., Gehrels, G.E., Karlstrom, K.E., Dickinson, W.R., Donahue, M.S., Gonzales, D.A., Blum, M.D., 2018. Provenance of Cretaceous through Eocene strata of the Four Corners region: Insights from detrital zircons in the San Juan Basin, New Mexico and Colorado. Geosphere 14 (2), 785–811.
Quinn, G.M., Hubbard, S.M., Putnam, P.E., Matthews, W.A., Daniels, B.G., Guest, B., 2018. A Late Jurassic to Early Cretaceous record of orogenic wedge evolution in the Western Interior basin, USA and Canada. Geosphere 14 (3), 1187–1206.
Reading, H.G. (Ed.), 2009. Sedimentary environments: processes, facies and stratigraphy. John Wiley & Sons.
Roberts, E.M., 2007. Facies architecture and depositional environments of the Upper Cretaceous Kaiparowits Formation, southern Utah. Sedimentary Geology 197 (3–4), 207–233.
Roca, X., Nadon, G.C., 2007. Tectonic control on the sequence stratigraphy of nonmarine retroarc foreland basin fills: Insights from the Upper Jurassic of central Utah, USA. Journal of Sedimentary Research 77 (3), 239–255.
Rossignol, C., Hallot, E., Bourquin, S., Poujol, M., Jolivet, M., Pellenard, P., Ducassou, C., Nalpas, T., Heilbronn, G., Yu, J., Dabard, M.P., 2019. Using volcaniclastic rocks to constrain sedimentation ages: To what extent are volcanism and sedimentation synchronous? Sedimentary Geology 381, 46–64.
Sames, B., Cifelli, R.L., Schudack, M.E., 2010. The nonmarine Lower Cretaceous of the North American Western Interior foreland basin: new biostratigraphic results from ostracod correlations and early mammals, and their implications for paleontology and geology of the basin—an overview. Earth-Science Reviews 101 (3–4), 207–224.
Sauer, K.B., Gordon, S.M., Miller, R.B., Vervoort, J.D., Fisher, C.M., 2017. Evolution of the Jura-Cretaceous North American Cordilleran margin: Insights from detrital-zircon U-Pb and Hf isotopes of sedimentary units of the North Cascades Range, Washington. Geosphere 13 (6), 2094–2118.
Schmitz, M.D., Schoene, B., 2007. Derivation of isotope ratios, errors and error correlations for U-Pb geochronology using ^{205}Pb-^{235}U-(^{233}U)-spiked isotope dilution thermal ionization mass spectrometric data. Geochemistry, Geophysics, Geosystems 8, Q08006. https://doi.org/10.1029/2006GC001492.
Scott, R.W., Oboh-Ikuenobe, F.E., Benson Jr., D.G., Holbrook, J.M., Alnahwi, A., 2018. Cenomanian-Turonian flooding cycles: US Gulf Coast and Western Interior. Cretaceous Research 89, 191–210.
Shang, F., Chen, R., Zhao, Z., Scott, R.W., Song, L., 2018. High-Precision Chronostratigraphic Correlation of Mid-Cretaceous Strata in Western Interior Basin, USA through Graphic Correlation Technique. Journal of Geoscience and Environment Protection 6 (5), 266.
Simmons, G.C., 1957. Contact of Burro Canyon Formation with Dakota sandstone, Slick Rock District, Colorado, and correlation of Burro Canyon Formation. AAPG Bulletin 41 (11), 2519–2529.
Skelton, P.W., Spicer, R.A., Kelley, S.P., Gilmour, I., 2003. The cretaceous world. The Cretaceous World. In: Skelton, Peter W., Spicer, Robert A., Kelley, Simon P., Gilmour, Iain (Eds.). Cambridge University Press, Cambridge, UK, p. 360, 0521831121.
Sláma, J., Košler, J., Condon, D.J., Crowley, J.L., Gerdes, A., Hanchar, J.M., Horstwood, M.S.A., Morris, G.A., Nasdala, L., Norberg, N., Schaltegger, U., Schoene, B., Tubrett, M.N., Whitehouse, M.J., 2008. Plešovice zircon — a new natural reference material for U-Pb and Hf isotopic microanalysis. Chemical Geology 241, 1–35.
Slattery, J.S., Cobban, W.A., McKinney, K.C., Harries, P.J., Sandness, A.L., 2015. Early Cretaceous to Paleocene paleogeography of the Western Interior Seaway: the interaction of eustasy and tectonism. Wyoming Geological Association Guidebook 2015, 22–60.
Sprinkel, D.A., Madsen, S.K., Kirkland, J.I., Waanders, G.L., Hunt, G.J., 2012. Cedar Mountain and Dakota formations around Dinosaur National Monument: evidence of the first incursion of the Cretaceous Western Interior Seaway into Utah. Utah Geological Survey 143.
Stokes, W.L., 1952. Lower Cretaceous in Colorado Plateau. AAPG Bulletin 36 (9), 1766–1776.
Suarez, C.A., González, L.A., Ludvigson, G.A., Cifelli, R.L., Tremain, E., 2012. Water utilization of the Cretaceous Mussentuchit Member local vertebrate fauna, Cedar Mountain Formation, Utah, USA: using oxygen isotopic composition of phosphate. Palaeogeography, Palaeoclimatology, Palaeoecology 313, 78–92.
Suarez, C.A., González, L.A., Ludvigson, G.A., Kirkland, J.I., Cifelli, R.L., Kohn, M.J., 2014. Multi-taxa isotopic investigation of paleohydrology in the Lower Cretaceous Cedar Mountain Formation, Eastern Utah, USA: deciphering effects of the Nevadaplano Plateau on regional climate. Journal of Sedimentary Research 84 (11), 975–987.
Szwarc, T.S., Johnson, C.L., Stright, L.E., McFarlane, C.M., 2015. Interactions between axial and transverse drainage systems in the Late Cretaceous Cordilleran foreland basin: evidence from detrital zircons in the Straight Cliffs Formation, southern Utah, USA. GSA Bulletin 127 (3–4), 372–392.
Suarez, M.B., Suarez, C.A., Al-Suwaidi, A.H., Hatzell, G., Kirkland, J.I., Salazar-Verdin, J., Ludvigson, G.A., Joeckel, R.M., 2017. Terrestrial Carbon Isotope Chemostratigraphy in the Yellow Cat Member of the Cedar Mountain Formation: Complications and Pitfalls. In: Terrestrial Depositional Systems. Elsevier, pp. 303–336.
Thomas, W.A., 2011. Detrital-zircon geochronology and sedimentary provenance. Lithosphere 3 (4), 304–308.
Tschudy, R.H., Tschudy, B.D., Craig, L.C., 1984. Palynological evaluation of Cedar Mountain and Burro Canyon Formations. Colorado Plateau. In: US Geological Survey Professional Paper, vol. 1281, p. 24.
Tucker, R.T., Roberts, E.M., Hu, Y., Kemp, A.I., Salisbury, S.W., 2013. Detrital zircon age constraints for the Winton Formation, Queensland: contextualizing Australia's Late Cretaceous dinosaur faunas. Gondwana Research 24 (2), 767–779.
Tucker, R.T., Roberts, E.M., Henderson, R.A., Kemp, A.I., 2016. Large igneous province or long-lived magmatic arc along the eastern margin of Australia during the Cretaceous? Insights from the sedimentary record. Bulletin 128 (9–10), 1461–1480.
Van Schmus, W.R., Bickford, M.E., Turek, A., Van der Pluijm, B.A., Catacosinos, P.A., 1996. Proterozoic geology of the east-central Midcontinent basement. SPECIAL PAPERS-GEOLOGICAL SOCIETY OF AMERICA, pp. 7–32.
Weishampel, D.B., Dodson, P., Osmólska, H., 2004. The Dinosauria, second ed. University of California Press, Berkeley, p. 880.
Whitmeyer, S.J., Karlstorm, K.E., 2007. Tectonic model for the Proterozoic growth of North America. Geosphere 3 (4), 220–259.
Willis, G.C., 1999. The Utah thrust system-an overview.
Wotzlaw, J.F., Hüsing, S.K., Hilgen, F.J., Schaltegger, U., 2014. High-precision zircon U–Pb geochronology of astronomically dated volcanic ash beds from the Mediterranean Miocene. Earth and Planetary Science Letters 407, 19–34.
Yingling, V.L., Heller, P.L., 1992. Timing and record of foreland sedimentation during the initiation of the Sevier orogenic belt in central Utah. Basin Research 4 (3-4), 279–290.
Zanno, L.E., Makovicky, P.J., 2011. On the earliest record of Cretaceous tyrannosauroids in western North America: implications for an Early Cretaceous Laurasian interchange event. Historical Biology 23 (4), 317–325.
Zanno, L.E., Makovicky, P.J., 2013. Neovenatorid theropods are apex predators in the Late Cretaceous of North America. Nature Communications 4, 2827.
Zanno, L.E., Makovicky, P.J., 2016. A new species of early diverging ornithopod increases the paleobiodiversity of herbivorous dinosaurs in Late Cretaceous ecosystems in North America. J Vert Paleontol Progr Abstr 2016, 256.

Zanno, L.E., Tucker, R.T., Canoville, A., Avrahami, H.M., Gates, T.A., Makovicky, P.J., 2019. Diminutive fleet-footed tyrannosauroid narrows the 70-million-year gap in the North American fossil record. Communications Biology 2 (1), 64.
Zimmermann, S., Mark, C., Chew, D., Voice, P.J., 2018. Maximising data and precision from detrital zircon U-Pb analysis by LA-ICPMS: the use of core-rim ages and the single-analysis concordia age. Sedimentary Geology 375, 5–13.

Appendix A. Supplementary data

Supplementary data to this article can be found online at https://doi.org/10.1016/j.cretres.2020.104384.